Propagation Models and Performance Evaluation for 5G Millimeter-Wave Bands

Shu Sun, *Student Member, IEEE*, Theodore S. Rappaport, *Fellow, IEEE*, Mansoor Shafi, *Life Fellow, IEEE*, Pan Tang, *Student Member, IEEE*, Jianhua Zhang, *Senior Member, IEEE*, and Peter J. Smith, *Fellow, IEEE*

***Abstract*—Fifth-generation (5G) wireless networks are expected to operate at both microwave and millimeter-wave (mmWave) frequency bands, including frequencies in the range of 24 to 86 GHz. Radio propagation models are used to help engineers design, deploy, and compare candidate wireless technologies, and have a profound impact on the decisions of almost every aspect of wireless communications. This paper provides a comprehensive overview of the channel models that will likely be used in the design of 5G radio systems. We start with a discussion on the framework of channel models, which consists of classical models of path loss versus distance, large-scale, and small-scale fading models, and multiple-input multiple-output channel models. Then, key differences between mmWave and microwave channel models are presented, and two popular mmWave channel models are discussed: the 3rd Generation Partnership Project model, which is adopted by the International Telecommunication Union, and the NYUSIM model, which was developed from several years of field measurements in New York City. Examples on how to apply the channel models are then given for several diverse applications demonstrating the wide impact of the models and their parameter values, where the performance comparisons of the channel models are done with promising hybrid beamforming approaches, including leveraging coordinated multipoint transmission. These results show that the answers to channel performance metrics, such as spectrum efficiency, coverage, hardware/signal processing requirements, etc., are extremely sensitive to the choice of channel models.**

***Index Terms*—Beamforming, channel models, coordinated multipoint (CoMP), hybrid beamforming, millimeter wave (mmWave), multiple-input multiple-output (MIMO), NYUSIM, fifth generation (5G).**

Manuscript received January 31, 2018; revised April 20, 2018; accepted May 22, 2018. Date of publication June 15, 2018; date of current version September 17, 2018. This work was supported in part by the NYU WIRELESS Industrial Affiliates program and in part by the NSF research under Grants 1320472, 1302336, and 1555332. The review of this paper was coordinated by Dr. Y. Fang. *(Corresponding author: Shu Sun.)*

S. Sun and T. S. Rappaport are with the NYU WIRELESS Research Center, Tandon School of Engineering, New York University, Brooklyn, NY 11201 USA (e-mail: ss7152@nyu.edu; tsr@nyu.edu).

M. Shafi is with the Spark New Zealand, Wellington 6011, New Zealand (e-mail: Mansoor.Shafi@spark.co.nz).

P. Tang and J. Zhang are with the State Key Laboratory of Networking and Switching Technology, Beijing University of Posts and Telecommunications, Beijing 100876, China (e-mail: tangpan27@bupt.edu.cn; jhzhang@bupt.edu.cn).

P. J. Smith is with the School of Mathematics and Statistics, Victoria University of Wellington, Wellington 6140, New Zealand (e-mail: peter.smith@msor.vuw.ac.nz).

Color versions of one or more of the figures in this paper are available online at http://ieeexplore.ieee.org.

Digital Object Identifier 10.1109/TVT.2018.2848208

I. Introduction

THE radio channel is fundamental to wireless communications. Almost every aspect of wireless communications, ranging from equipment design and system design to system performance, depends upon an accurate understanding of the performance of radio signals when they propagate via a radio channel. The modeling of a radio channel is therefore vital to wireless communications research [1]. The demand for cellular data traffic continues to outstrip forecasts and is currently growing at a rate of 40–70% per annum [2]. This growth rate implies that relative to current levels, a 1000 times capacity increase within the next decade may be required to be met by the new radio capabilities of the fifth-generation (5G) wireless communications [3]. The capacity gains required by 5G are expected to be provided by:

- Massive multiple-input multiple-output (MIMO) antenna arrays at base stations (BSs) and smaller arrays at the mobile user equipment (UE) [4]
- Increased spectrum bandwidth and use of wideband ($>$ 100 MHz) channels
- Multi-user and three-dimensional (3D) MIMO [5]
- Network densification using smaller cell coverage zones [6]
- New modulation waveforms

A discussion of the above is given in [7] and references therein, but it is clear that new waveforms will offer the smallest capacity increase, while increased spectrum bandwidth and channel bandwidth using directional antennas will provide the largest capacity increases. With dense networks, capacity increases in conventional ultra-high frequency (UHF)/microwave networks, interference will be the limiting factor, thus the peak rates cannot be achieved [7]. Furthermore, according to the International Telecommunication Union (ITU) requirement for compliance with International Mobile Telecommunications-2020 performance [8], no amount of densification can yield the target peak rates of 20 Gbps and per-user rates of 100 Mbps at the 5% cumulative distribution function (CDF) level, unless much larger bandwidths are made available. However, increased spectrum bandwidth cannot come from existing microwave bands which are already congested and allocated for other purposes, thus new millimeter-wave (mmWave) spectrum bands of 30–300 GHz are being considered for 5G and beyond, since they have ample unused spectrum relative to the microwave bands [9] and are potential candidates for allocation to mobile services. The World Radio Conference in 2015 (WRC-15) approved a number of candidate bands for 5G, which

are: 24.25–27.5 GHz, 31.8–33.4 GHz, 37–43.5 GHz, 45.5–50.2 GHz, 50.4–52.6 GHz, 66–76 GHz, and 81–86 GH. A final list of the bands will be approved by WRC-19. In addition to these bands, spectrum in the 60 GHz band may also be used. A judicious contribution of spectrum use across all bands is necessary to keep up with capacity demands, and this also is likely to include lower UHF/microwave frequencies for wider area coverage.

Due to the importance of mmWave channel modeling and the novelty of using frequencies above 6 GHz for mobile communications, many different groups around the world have embarked on sharing knowledge and producing mmWave channel models, such as the 3rd Generation Partnership Project (3GPP) (for 0.5–100 GHz) [10], [11], the ITU (for 0.5–100 GHz) [8], [12], European Cooperation in Science and Technology (COST) 2100 (applicable frequencies not specified), the Mobile and Wireless Communications Enablers for the Twenty-Twenty Information Society (METIS) (up to 70 GHz for a stochastic model, and up to 100 GHz for a map-based model[1]) [13], 5G mmWave Channel Model Alliance (for 0.5–100 GHz) [14], Fraunhofer HHI (which developed QUAsi Deterministic RadIo channel GenerAtor (QuaDRiGa)) (applicable frequencies not specified) [15], NYU WIRELESS (for 0.5–100 GHz) [16], IEEE 802.11 ad/ay (for the 60 GHz band) [17], IEEE 802.15.3d (for the 300 GHz band) [18], IEEE 802.15.3e (for the 60 GHz band) [19], Millimeter-Wave Evolution for Backhaul & Access (MiWEBA) (up to the 60 GHz band) [20], mmWave based Mobile Radio Access Network for 5G Integrated Communications (mmMAGIC) (for 6–100 GHz) [21], a consortium of universities and industry, and many individually led efforts [22]–[25]. Many of the participants of these global groups participate overlap with the organizations, thus there is a great deal of similarity in models in many cases. The statistical channel models proposed by those different groups can be boiled down to 3GPP/ITU and NYUSIM channel models [16], [26]. Therefore, we compared the performance of 5G systems using these two models. Nevertheless, our methodology can be extended to other models.

The main purpose of the 3GPP [11] and ITU statistical models [8], [27] is to enable simulations for 5G candidate technology evaluations, and, importantly, to include the effects of directional, steerable antennas that will be needed for practical mobile systems at mmWave frequencies [28], [29]. It is desirable, but not a primary function, of these models to accurately predict real-world system performances. However, certain parts of 3GPP, such as RAN4,[2] will require models that accurately predict mmWave MIMO performance in the face of interference, since antenna directionality will directly impact interference. It is fair to say that the 3GPP and ITU models for frequencies above 6 GHz are in their early stages of development, and their use for research should be tempered with caution [16]. This motivates us to prepare this paper to show that the impact of channel model choice is extremely wide ranging. To demonstrate this fact, we present a number of examples and carefully compare results using the 3GPP/ITU model [8], [11] and NYUSIM model [16], where promising hybrid beamforming (HBF) approaches are used to investigate channel performance [28]. Note that in this work, we are not advocating one channel model over another, as both models are in use widely throughout the community. Rather, we are illustrating how different channel models impact system performance results, and we attempt to solve the issue of determining the system capacity and impact of various algorithms and various antenna structures in a multi-user multi-stream system using two different channel models, in order to provide a range of results that may be of use to the wireless research community. The purpose of this paper is to not create channel models, rather to implement systems.

The key contributions of this paper include examples of methodologies/simulations/calculations on how to apply the channel models to evaluate 5G mmWave system performance, and demonstration of the wide ranging results produced. The most remarkable results are as follows:

- In the case of cell range prediction, the different large-scale path loss models and shadow fading values in both channel models lead to a noticeable difference on the cell range evaluation given a certain cell-edge signal-to-noise ratio (SNR).
- In terms of the eigenvalue properties of the channel, one model predicts significantly more dominant eigen modes than the other. This implies that the spatial degrees of freedom predicted by both channel models are quite different, hence resulting in different numbers of available spatial streams to be multiplexed.
- In terms of spectrum efficiency, the performance of a single-cell single-user is a base case. Which channel model predicts higher spectral efficiency depends on the number of transmitted data streams, and NYUSIM predicts a much higher occurrence of peak rates than the 3GPP model when the number of data streams is small (e.g., no more than four).
- Extending the single-cell case to a multi-cell multi-user case, we propose a new HBF approach. The novelty of the proposed approach, called signal-to-leakage-plus-noise-ratio (SLNR)-based HBF, as opposed to the algorithm in [30] is that the SLNR-based HBF consists of both RF analog beamforming and digital baseband beamforming, rather than digital-only processing as considered in [30], and that a CoMP technique, named coordinated beamforming, is utilized in this work. Here we show that the median values of per-user spectrum efficiency is roughly half for the 3GPP model relative to the NYUSIM model when there are a relatively small number of RF chains at each BS.
- The number of RF chains needed to achieve a given spectrum efficiency level is a key parameter to determine TX and RX signal processing requirements. Here we show that for the multi-cell case the median spectrum efficiency for the 3GPP models even with 2.5 times more RF chains is still less than what is predicted by the NYUSIM model. Less RF chains means less RF hardware, less power consumption and lower cost.

[1]A map-base model is built upon the geometry of objects, such as buildings and streets, and transmitter (TX) and receiver (RX) locations in the area under study, and is usually only applicable to a specific environment.

[2]RAN4 refers to Radio Access Network working group 4, which performs simulations of diverse radio frequency (RF) system scenarios and derives the minimum requirements for transmission and reception parameters, and for channel demodulation. Once these requirements are set, the group defines the test procedures that will be used to verify them (only for BS).

II. Channel Model Framework

A. Path Loss and Large-Scale Fading

Path loss is the reduction in power density of a radio wave as it propagates through the channel, which is defined as [31]

$$\mathrm{PL[dB]} = 10\log_{10}\frac{P_{\mathrm{T}}}{P_{\mathrm{R}}}, \tag{1}$$

where P_{T} and P_{R} are the transmitted and received power, respectively. In free space, the received power is a function of distance and wavelength/frequency, also known as Friis' law

$$P_{\mathrm{R}}(d,\lambda) = P_{\mathrm{T}}G_{\mathrm{T}}G_{\mathrm{R}}\left(\frac{\lambda}{4\pi d_{3\mathrm{D}}}\right)^2, \tag{2}$$

where G_{T} and G_{R} are the antenna gains at the TX and RX, respectively, λ is the wavelength, d_{3D} is the spatial distance between the TX and RX. However, in real environments, there are many dielectric and conducting obstacles and path loss is more severe than in free space, thus a lot of effort has been devoted to field measurements and path loss modeling. Several empirical path loss models have been widely used for frequencies below 6 GHz [12], [27]. Similarly, for mmWave, numerous field measurements have been carried out in the 28, 38, 60, 73, and 80 GHz bands. Two main types of path loss models for mmWave channels, along with their corresponding shadow fading values, have been proposed and used by researchers and standards bodies [32], [33], i.e., the alpha-beta-gamma (ABG) model, and the close-in (CI) free space reference distance model, which are detailed in Section IV-B.

B. Small-Scale Fading

Small-scale fading is involved in the channel impulse response (CIR). For a narrowband flat fading channel, the CIR can be described as

$$h(t,\tau) = V + g(t,\tau), \tag{3}$$

where V is a complex and deterministic component, which exists in the line-of-sight (LOS) case with a strong and dominant path between the TX and RX. If we assume the multiple received radio waves are wide-sense stationary uncorrelated scattering (WSSUS), $g(t,\tau)$ is typically a complex zero-mean Gaussian random variable with its envelope obeying the Rayleigh distribution. However, if there is a fixed LOS component, the amplitude obeys the Ricean distribution. As the channel bandwidth increases, the RX can resolve multiple paths according to their delays and the CIR will change to

$$h(t,\tau) = V\delta(\tau-\tau_0) + \sum_{i=1}^{N} g_i(t)\delta(\tau-\tau_i), \tag{4}$$

where $g_i(t)$ is a complex Gaussian variable with the excess delay τ_i, $\delta(\cdot)$ is the Dirac function and N is the number of resolvable delay bins. This tapped delay line (TDL) model can describe the channel variation in delay dispersion. However, as the channel bandwidth increases from 5 MHz to 20 MHz, even to 100 MHz, the delay resolution is also enhanced significantly and more multipaths can be expected.

The Geometry-based Stochastic Channel Model (GSCM) is another modeling method (used in the COST modeling framework) [34], in which the geometric position of scatterers is determined by a probability density function and ray tracing is used to determine the actual double-directional impulse response. Furthermore, large-scale parameters and small-scale parameters are proposed to describe the GSCM. Fig. 1(a) illustrates the GSCM/COST model. The rays depart from the TX, propagate through the channel, and finally arrive at the RX. In the spherical coordinates, the angle-of-departure (AoD) and angle-of-arrival (AoA) at both TX and RX sides are used to characterize the rays. Furthermore, a cluster generally consists of rays, which come from the same scatterer (e.g., a group of buildings), with similar characteristics, e.g., delays, AoDs and AoAs.

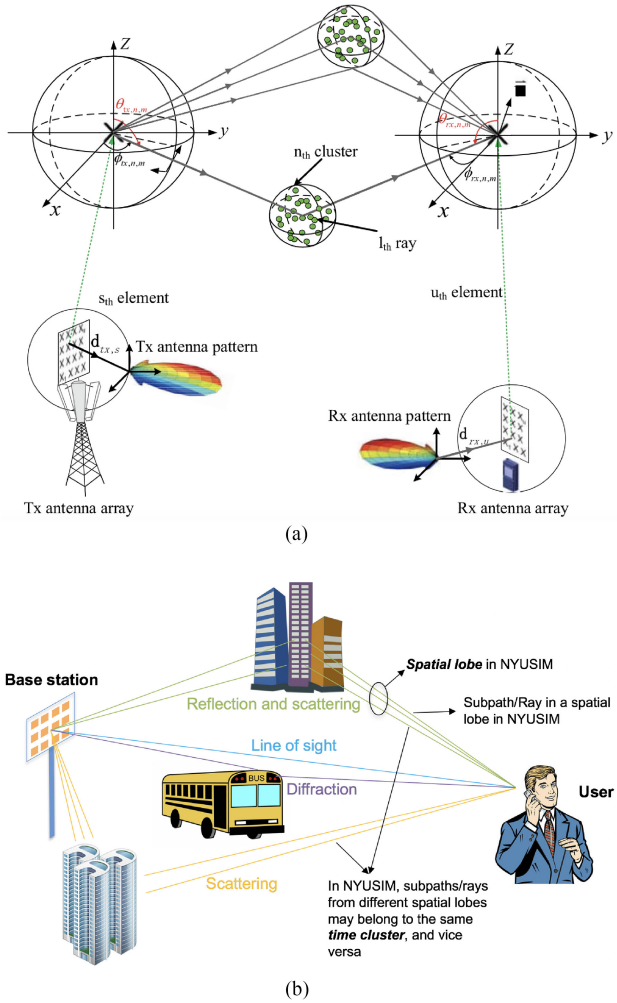

Fig. 1. Illustration of 3D MIMO channel in the (a) GSCM/COST and (b) NYUSIM model.

Note that in the NYUSIM channel model, clusters are composed of multipath components (MPCs) traveling close in time (i.e., time clusters), and MPCs with common propagation directions are regarded as being contained in a spatial lobe, as demonstrated in Fig. 1(b). Unlike the common GSCM/COST model, where a joint distribution in space and time is imposed on each individual MPC, the NYUSIM approach allows the time clusters and spatial lobes to be separately distributed, such that total energy in time equals total energy over space, but where the arrivals and time delays are statistically distributed, and not forced to have a joint distribution in the model.

III. MmWave and Microwave Model Differences

Due to the increase in frequency, radio waves with high frequency have different propagation characteristics compared to microwave. For example, mmWaves can not efficiently penetrate and diffract around obstacles, e.g., cars, buildings and people. This results in less diffracting MPCs and high path loss. In the following subsections, we focus on several channel properties in mmWave bands and discuss new requirements for channel models.

A. Attenuation and Blockage

During propagation, mmWaves may be partially or totally absorbed by an absorbing medium, which results in additional loss. Thus, rain attenuation and atmospheric attenuation [35] should be considered in mmWave systems, although this is not a concerned problem in microwave systems. Additionally, mmWave systems are much more sensitive to blockage by obstacles. In [36], it was found that outdoor tinted glass had a penetration loss of 40.1 dB at 28 GHz, and three interior walls of an office building had a penetration loss of 45.1 dB, with a distance of 11.39 m between the TX and RX. If stationary or moving objects stand between the TX and RX, channel characteristics will be dramatically changed when the signal is blocked, especially for mmWave channels. The shadowing caused by these objects is important for the link budget and the time variance of the channel. Furthermore, such dynamic blocking is perhaps important to capture in evaluations of technologies, e.g., beam-finding and beam-tracking capabilities.

B. Channel Sparsity

It is usually claimed that mmWave channels are sparse in the angle and delay domains [37]. For example, in [38], only up to five spatial lobes are found in dense-urban non-line-of-sight (NLOS) environments, and the delay/angle spreading within each cluster is relatively small. However, more experimental verifications of this are needed. Nonetheless, a lower bound on the channel sparsity can still be established based on existing measurements, and in many environments the percentage of delay/angle bins with significant energy is rather low while it is higher at centimeter-wave frequencies.

C. Large Bandwidth and Large Antenna Arrays

To meet the demand of future mobile data growth [39], bandwidths on the order of 1 GHz are needed. In mmWave bands, there are large bandwidths available, and smaller wavelengths make large antenna arrays feasible [40]. Thus, the channel model should consider high resolution in both delay and angular domains. In order to model this effect, the offset spatial angles and relative time delays of rays within a cluster should be modeled as a variable rather than constant. Various types of antenna arrays, such as the uniform linear array (ULA) and uniform rectangle array (URA), are being considered.

D. Spatial Consistency

Spatial consistency is identified as an important feature for 5G channel models. The spatial consistency of a channel means that the channel evolves smoothly without discontinuities when the TX and/or RX moves or turns. It also means that channel characteristics in closely located users are highly correlated. Spatial consistency covers various aspects, e.g., large-scale parameters and small-scale parameters of delays, AoAs and AoDs, outdoor/indoor state, and LOS/NLOS state. In [11], a spatial consistency procedure is used for both cluster-specific and ray-specific random variables to be spatially consistent.

E. Stationarity Regions

A stationarity region denotes a spatial or temporal region within which the correlation coefficient of the targeted channel properties is above a certain threshold (between 0 and 1), i.e., allowance of similarity level (ASL) (there is no uniform standard on the value of the ASL) [41], [42]. The study of channel stationarity plays an important role in channel modeling and estimation, since stationarity has to be assumed in order to obtain accurate estimates and reproduce channel parameters. Measurements at 2 GHz to 30 GHz have indicated that the spatial stationarity regions of mmWave bands (less than 0.09 m or so) are much smaller than those at UHF/microwave frequencies (around 0.6 m) for an ASL of 0.6 [41], [42]. Furthermore, recent field measurements have shown very sharp spatial decorrelation over small distance movements of just a few tens of wavelengths at mmWave frequencies, yet it is noteworthy that the orientation of directional antennas with respect to the surrounding environment can impact the stationarity and correlation distances [42]. Therefore, stationarity regions need to be carefully characterized in 5G channel modeling that incorporates mmWave bands.

F. Random Cluster Numbers

In the existing channel model for microwave bands, the number of clusters is a constant [27]. For the mmWave bands, this assumption may not be reasonable. According to recent literature, cluster/time-cluster numbers are small and random, and are well-modeled by a Poisson distribution [37], [38]. In [43], the mean cluster number is 12 while it is less than 4 in [37] (Note that the definition of cluster is different in these two references). By making the cluster numbers random, some channel properties, e.g., capacity, will change correspondingly. This is further discussed in later sections of this paper.

IV. 3GPP and NYUSIM Channel Models

This section introduces and compares two channel models that will be employed in the simulations in this paper: the channel model in the 3GPP TR 38.901 Release 14 [11], and the statistical spatial channel model (SSCM) NYUSIM proposed by New York University (NYU) [16], [38]. Parameters of these two channel models are given in [11] and [38], [44].

A. LOS Probability Model

LOS probability denotes the probability that a given user terminal (UT) or UE is in a LOS condition with respect to the BS. LOS probability models in 3GPP [11] and NYUSIM [16] channel models for urban microcell (UMi) and urban macrocell (UMa) scenarios are contained in [45, Tables I and II], respectively.

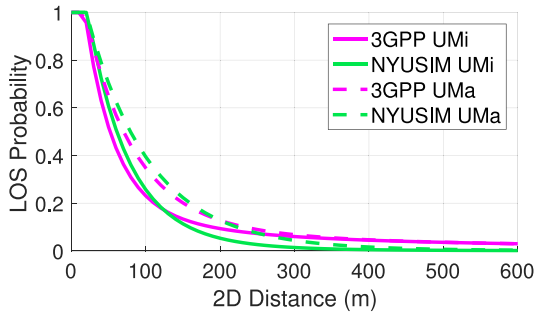

Fig. 2. Comparison of LOS probability models in the 3GPP channel model [11] and NYUSIM [16] in UMi and UMa scenarios for a UE height of 1.5 m.

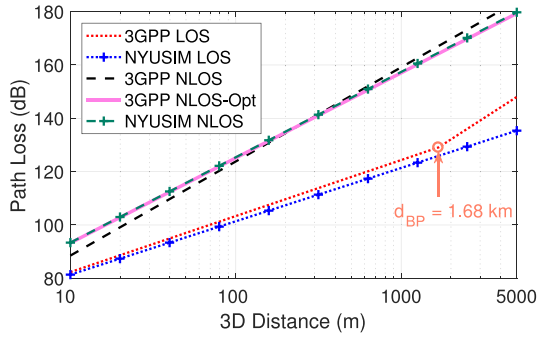

Fig. 3. Path loss models in the 3GPP channel model and NYUSIM in UMi LOS and NLOS scenarios for a BS height of 10 m and a UE height of 1.5 m. "Opt" denotes the optional NLOS CI path loss model in the 3GPP channel model.

Fig. 2 illustrates the LOS probability models in the 3GPP and NYUSIM channel models in UMi and UMa scenarios for a UE height of 1.5 m. As shown by Fig. 2, the 3GPP LOS probability model has clearly a non-zero tail at large distances (several hundred meters), which is not likely to be true in urban environments where numerous tall buildings exist, while NYUSIM shows essentially zero probability at large distances in urban areas which is different from the 3GPP model. On the other hand, for T-R separation distances smaller than about 120 m (for UMi) or 160 m (for UMa), NYUSIM predicts a larger LOS probability compared to 3GPP. Through 1000 random channel simulation runs for the UMi street canyon scenario over distances from 10 m to about 300 m (where cell size was based on the condition that 95% of the area within a cell has an SNR $\geq$ 5 dB, detailed in Section V-B), the simulated LOS probability is 9.1% and 17.2% using 3GPP and NYUSIM models, respectively. The difference in the LOS probability impacts spectral efficiency, since LOS facilitates stronger mmWave propagation (i.e., larger SNR) compared to the NLOS condition due to more severe diffraction loss at mmWave frequencies than at sub-6 GHz.

B. Large-Scale Path Loss Model

For a communication link with TX power $\mathrm{P_T}$, the received power $\mathrm{P_R}$ [dBm] = $\mathrm{P_T}$ [dBm] + $\mathrm{G_T}$ [dB] + $\mathrm{G_R}$ [dB] - PL [dB] [31], where $\mathrm{G_T}$ and $\mathrm{G_R}$ are the TX and RX antenna gain, respectively, and PL denotes the large-scale path loss. Large-scale path loss models in 3GPP and NYUSIM are listed and compared in [45, Tables IV and V] for the UMi and UMa scenarios, respectively, where the CI models in 5GCM represent the path loss models in NYUSIM. In general, there are two types of large-scale path loss models as mentioned in Section II-A: a physics-based CI model and a mathematically based ABG model. The expressions for ABG and CI models are given by (1) and (2) in [33], respectively, and thorough discussions on advantages, drawbacks, prediction accuracy, and parameter stability of these path loss models are also provided in [33].

In the 3GPP model, the CI path loss model is utilized for $d_{3\mathrm{D}}$ smaller than the breakpoint distance d_{BP}. After the breakpoint distance, a new term involving the BS and UE heights is added to the CI model, where the BS height is set to 10 m, and the UE height ranges from 1.5 m to 22.5 m. In the UMi street canyon NLOS scenario, the ABG path loss model is adopted with a term accounting for the UE height added to it, while the CI model is listed as an optional path loss model. In NYUSIM, the single-slope CI model is employed since breakpoints were never observed in outdoor measurements in Manhattan or Austin.

When comparing the 3GPP ABG path loss model with the CI model, the ABG model is based on a regression fit to path loss versus distance for various bands and this is used to derive the three modeling parameters, but this can lead to accuracy issues as demonstrated in [33]. The 1-m CI model used in NYUSIM and the optional 3GPP model has fewer parameters, and offers intuitive appeal, better model parameter stability, and higher accuracy over a wide range of microwave and mmWave bands, scenarios, and distances [33]. Fig. 3 illustrates the path loss models in the 3GPP channel model and NYUSIM in UMi LOS and NLOS scenarios for a BS height of 10 m and a UE height of 1.5 m. Fig. 3 shows that for the UMi LOS scenario, the 3GPP ABG model predicts larger path loss as compared to the NYUSIM CI model, and there exists an extremely large breakpoint distance of 1.68 km which well exceeds typical UMi cell sizes hence reverting the double-slope model to a single-slope model. For the NLOS environment, the 3GPP ABG model predicts less mean path loss for T-R separation distances smaller than 296 m when compared with the NYUSIM CI model. On the other hand, the 3GPP optional NLOS CI model matches the NYUSIM NLOS CI model very well.

C. Outdoor-to-Indoor (O2I) Penetration Loss Model

1) O2I Penetration Loss Model in the 3GPP Channel Model: In the 3GPP channel model, the overall path loss (especially for indoor users) mainly consists of three parts: outdoor path loss, O2I penetration loss, and indoor path loss, which is modeled as [11]

$$\mathrm{PL\ [dB]} = \mathrm{PL}_b + \mathrm{PL}_{tw} + \mathrm{PL}_{in} + N(0, \sigma_P^2) \tag{5}$$

where PL_b is the basic outdoor path loss, PL_{tw} is the building penetration loss through the external wall, PL_{in} is the indoor loss which depends on the depth into the building, and σ_P is the standard deviation for the penetration loss. The building penetration loss PL_{tw} has the following form

$$\mathrm{PL}_{tw}\ [\mathrm{dB}] = \mathrm{PL}_{npi} - 10\log_{10}\sum_{i=1}^{N}\left(p_i \times 10^{-\frac{L_{\mathrm{material}_i}}{10}}\right) \tag{6}$$

where PL_{npi} is an additional loss added to the external wall loss to account for non-perpendicular incidence, which is 5 dB

in the 3GPP channel model. $L_{\text{material}_i} = a_{\text{material}_i} + b_{\text{material}_i} \cdot f_c$ is the penetration loss of material i, f_c is the frequency in GHz, p_i is the proportion of the i-th material, where $\sum p_i = 1$, and N is the number of materials. Penetration loss of several materials and the O2I penetration loss models are given in [45, Tables IX and X], respectively.

Two variants of the O2I penetration model are provided: a low-loss and a high-loss model. The composition of low and high loss is a simulation parameter to be determined by channel model users, and is dependent on the use of metal-coated glass in buildings and the deployment scenarios [11]. Both low-loss and high-loss models in the 3GPP channel model are applicable to UMa and UMi street canyon scenarios, whereas only the low-loss model is applicable to RMa [11].

2) O2I Penetration Loss Model in NYUSIM: In NYUSIM, a very succinct parabolic model with a good fit for predicting building penetration loss (BPL) of either high loss or low loss buildings was provided in [14] as

$$\text{BPL [dB]} = 10\log_{10}(A + B \cdot f_c^2) \tag{7}$$

where f_c is in GHz, $A = 5$, and $B = 0.03$ for low loss buildings, and $A = 10$ and $B = 5$ for high loss buildings.

D. Cluster Definition

This subsection introduces the cluster definition and clustering algorithm in the 3GPP and NYUSIM channel models.

1) Cluster Definition in the 3GPP Channel Model: In the 3GPP channel model [11], clusters are characterized by a *joint* delay-angle probability density function, such that a group of traveling MPCs must depart and arrive from a unique AoD-AoA combination centered around a mean propagation delay [11], [38].

2) Cluster Definition in NYUSIM: NYUSIM uses *time cluster* and *spatial lobe* concepts to describe multipath behavior for omnidirectional and directional CIRs [16], [38]. Time clusters are composed of MPCs traveling close in time, and arriving from potentially different directions in a short propagation time window. Spatial lobes denote primary directions of departure (or arrival) where energy arrives over several hundred nanoseconds or more [38]. A time cluster contains MPCs traveling close in time, but may arrive from different spatial lobe angular directions, such that the temporal and spatial statistics are decoupled and can be recovered separately. Similarly, a spatial lobe may contain many MPCs arriving (or departing) in a space (angular cluster) but with different time delays. Both clustering strategies described above are based on measurements, which are then processed differently to form different cluster models.

E. Large-Scale Parameters

1) Large-Scale Parameters in the 3GPP Channel Model: In the 3GPP channel model [11], large-scale parameters (LSPs) mainly include delay spread (DS), angular spreads (ASA, ASD, ZSA, ZSD), Ricean K-factor (K) and shadow fading (SF) taking into account cross correlation [11]. These LSPs act as fundamental channel modeling parameters and play a key role in generating other relevant channel modeling parameters such as small-scale parameters (SSPs). The LSPs and their statistics in the 3GPP channel model are provided in [11, Table 7.5–6].

2) Large-Scale Parameters in NYUSIM: [44, Table I] shows the LSPs and their statistics at various mmWave frequencies in NYUSIM. In addition to the statistics of LSPs in the log scale as given in the 3GPP model, NYUSIM also provides the statistics in their regular units, such as nanoseconds for delay spread, and degrees for angular spreads, which is more intuitive [44].

F. Small-Scale Parameters

1) Small-Scale Parameters in the 3GPP Channel Model: These are cluster excess delays, cluster powers, and cluster arrival angles and departure angles for both azimuth and elevation. Key channel modeling parameters for generating SSPs are listed in [11, Table 7.5–6].

2) Small-Scale Parameters in NYUSIM: Since the cluster definitions in the 3GPP channel model [11] and NYUSIM [38] are discrepant, SSPs in NYUSIM are also a little different from those in the 3GPP channel model. In NYUSIM, SSPs include time cluster excess delays, time cluster powers, and mean AoD and AoA azimuth and elevation angles for each spatial lobe. Key channel modeling parameters for generating SSPs in NYUSIM are given by [44, Table III].

It is worth noting that the number of clusters and the number of rays per cluster in the 3GPP channel model have fixed values, whereas the number of time clusters, the number of subpaths per time cluster, and the number of spatial lobes (both departure and arrival) in NYUSIM do not hold particular values but follow certain distributions and can vary in each channel realization. Furthermore, the numbers of clusters in the 3GPP model are much higher as compared to the measured numbers of time clusters (around 3 to 4 on average) and spatial lobes (about 2 on average) in NYUSIM. Those differences lead to a significant difference in channel sparsity predicted by the two channel models, and have a huge impact on spectral efficiency evaluation, as will be demonstrated later by simulation results.

G. Cross-Correlations

Cross-correlation coefficients between various channel modeling parameters in 3GPP and NYUSIM are displayed in [11, Table 7.5–6] and [44, Table II], respectively.

H. Channel Eigenvalues

Channel eigenvalues are a measure of the number of eigen channels for spatial multiplexing in a MIMO system. We generate the downlink $N_{\text{R}} \times N_{\text{T}}$ MIMO channel matrix $\mathbf{H}$ using both 3GPP [11] and NYUSIM [16], [38], [44] channel models, for a system operating at 28 GHz with 100 MHz RF bandwidth, and 256 BS antennas and 16 MS antennas, composing a URA in the x-z plane on each side. Simulation settings are detailed in Table I. The eigenvalues of $\mathbf{HH}^H$ are calculated and compared, and normalized eigenvalue magnitudes are obtained as follows

$$\eta_i = \frac{\eta_i'}{\sum_{i=1}^{N_{\text{R}}} \eta_i'} \tag{8}$$

where η_i denotes the i-th largest normalized eigenvalue of $\mathbf{HH}^H$, and η_i' is the i-th largest eigenvalue of $\mathbf{HH}^H$.

Fig. 4 depicts the CDFs of the largest four channel eigenvalues of $\mathbf{HH}^H$ (with the superscript H denoting conjugate transpose)

TABLE I
SIMULATION SETTINGS FOR COMPARING CHANNEL EIGENVALUES AND SPECTRAL EFFICIENCIES BETWEEN THE 3GPP CHANNEL MODEL [11] AND NYUSIM [16]

Parameter	Setting
Carrier Frequency	28 GHz
Base Station Transmit Power	+46 dBm
95% Cell-Edge SNR	5 dB
BS Antennas	uniform rectangular array consisting of N_{T} cross-polarized elements in the x-z plane
BS Antenna Spacing	half wavelength
BS Antenna Element Gain	8 dBi [11]
BS Antenna Element Pattern	Model 2, Page 18 in 3GPP TR 36.873 Release 12 [10]
MS Antennas	uniform rectangular array consisting of N_{R} cross-polarized elements in the x-z plane
MS Antenna Spacing	half wavelength
MS Antenna Element Gain	0 dBi
MS Antenna Element Pattern	omnidirectional
Receiver Noise Figure	10 dB

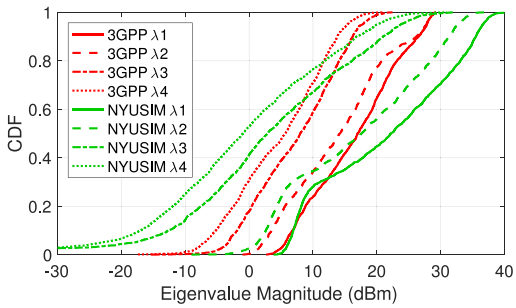

Fig. 4. CDFs of the largest four channel eigenvalues at 28 GHz in 3GPP and NYUSIM channel models for each individual user in a single-cell three-user MIMO system in the UMi scenario. The transmit and receive antenna arrays are uniform rectangular array composed by 256 and 8 cross-polarized elements, respectively.

for both 3GPP [11] and NYUSIM [16], [38] for each individual user in a single-cell three-user MIMO system in the UMi scenario. It is observed from Fig. 4 that the highest two eigenvalues in NYUSIM are larger than those in 3GPP, while the third and fourth eigenvalues are smaller most of the time. This indicates that NYUSIM yields only a few but strong dominant eigenmodes, whereas the 3GPP model generates more eigenmodes with weaker powers. The number of dominant eigen channels (i.e., the channel rank) in NYUSIM is statistical and can vary over the range of 1 to 5, where 5 is the maximum number of spatial lobes [38], with an average and typical value of 2.

Fig. 5 illustrates the average normalized eigenvalue magnitude of $\mathbf{HH}^H$ as a function of the eigenvalue index for both 3GPP [11] and NYUSIM [16], [38] models, where the normalized eigenvalue magnitude is obtained by dividing the eigenvalue by the sum of all the eigenvalues in linear scale of a channel matrix. As shown by Fig. 5, the first two dominant eigen channels of 3GPP and NYUSIM channel models are roughly equal in normalized magnitude. Furthermore, all the eigenvalues of the 3GPP channel are within 25 dB of the largest eigenvalue.

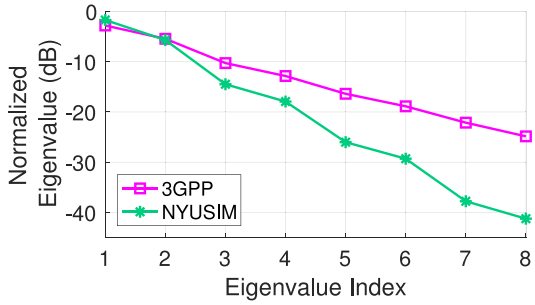

Fig. 5. Comparison of normalized channel eigenvalues at 28 GHz in 3GPP and NYUSIM channel models for each individual user in a single-cell three-user MIMO system in the UMi street canyon scenario. The transmit and receive antenna arrays are uniform rectangular array composed by 256 and 8 cross-polarized elements, respectively.

On the contrary, for NYUSIM, only four normalized eigenvalues are greater than -25 dB, and the non-dominant eigenvalue magnitudes decrease rapidly. This indicates the sparse feature of the mmWave channel such that the number of available spatial multiplexing streams is relatively limited. This is likely caused by the small number of clusters and narrow angular spreads modeled in mmWave channels by NYUSIM.

While the above results are for UMi and UMa scenarios, recent mmWave indoor channel measurements and modeling work in [46] shows four (LOS) and six (NLOS) time clusters, which are much smaller than in the 3GPP model [11] and are closer to the numbers of time clusters in NYUSIM for UMi and UMa scenarios, and very comparable to indoor data presented in [47]. This implies that the 3GPP model differs somewhat from real-world measured channels for the indoor scenario in [46], [47]. Spectral efficiency calculation for mmWave indoor channels, and development of indoor channel models for NYUSIM is currently ongoing.

V. EXAMPLES AND APPLICATIONS

A. Mobile System Coverage and Performance Studies

Let us assume a single-cell MU-MIMO system operating at 28 GHz with an RF bandwidth of 100 MHz in the UMi street canyon scenario. Even though 5G wireless systems will have large bandwidths (up to 1 GHz), this bandwidth is likely to be aggregated over component carriers each 100 MHz wide. Bandwidths larger than 100 MHz would result in a large SNR decrease at the cell edge. One can assume MIMO-OFDM modulation where the 100 MHz RF bandwidth is divided into K OFDM narrowband sub-carriers stacked in a wide band, the frequency-domain channel response at each sub-carrier can be obtained via the method shown on [31, p. 83]. However, as this work focuses on HBF performance evaluation, a single sub-carrier frequency of 28 GHz with a frequency-flat fading (i.e., narrowband approximation) channel is assumed for ease of analysis, while wideband implementation with MIMO-OFDM modulation is an interesting topic for future work. The BS is equipped with N_{T} cross-polarized antenna elements comprising a URA (where $N_{\mathrm{T}}/2$ elements are $+45^{\circ}$ slanted, and the other $N_{\mathrm{T}}/2$ are -45° slanted). There are three UEs in the cell, and each UE has eight cross-polarized omnidirectional antenna elements constituting a URA (where four elements are $+45^{\circ}$

slanted, and the other four are -45° slanted). The spacing between adjacent co-polarized elements is $\lambda/2$ with λ denoting the carrier wavelength (e.g., 10.7 mm at 28 GHz). Cross-polarized antenna elements are considered herein since they can effectively reduce the physical size while making use of different polarization components. Each BS antenna element has a radiation pattern as specified in [11, Table 7.3–1] with a maximum gain of 8 dBi, which provides a 3 dB beamwidth resolution of about 8.6° in the broadside direction of the URA. Each RX antenna element possesses an omnidirectional pattern. The total transmit power in a cell is 46 dBm which is equally shared by the three users in the cell. In the simulations, it is assumed that 95% of the area in the cell has an SNR larger than or equal to 5 dB, and the downlink cell radius is calculated based on this assumption, while also assuming an omnidirectional antenna pattern (i.e., zero gain) at the receiver through application of (9) [31]

$$\mathrm{PL}(f_c, d_{\max})[\mathrm{dB}] = \mathrm{P_T} + \left(10\log_{10} N_{\mathrm{T}} + \mathrm{G_T}\right) - \mathrm{N_0} - \mathrm{SNR_{cell\text{-}edge}} \quad (9)$$

where $\mathrm{P_T}$ represents the transmit power for each user in dBm, $\mathrm{G_T}$ is the gain of each BS TX antenna element in dBi, $\mathrm{N_0}$ denotes the noise power in dBm, and $\mathrm{SNR_{cell\text{-}edge}}$ is the cell-edge SNR in dB, which is 5 dB in our simulations. Note that $10\log_{10} N_{\mathrm{T}}$ represents the boresight array gain [48], and the array gain for directions other than the boresight is smaller than this value, dependent on the array factor of the particular antenna pattern. In general, the antenna array gain on boresight is approximately proportional to the number of antenna elements, but also depends on the radiation angle, and the specific gains and patterns of the antenna elements [49]. At the cell edge, the boresight array gain is the key factor for coverage, as sidelobes off of the main beam will be far below the boresight power levels [49]. The most vital term in Eq. (9) is $\mathrm{PL}(f_c, d_{\max})$, which denotes the large-scale path loss in dB at the cell edge $d_{\max}$, and should correspond to an SNR no smaller than the cell-edge SNR 95% of the time statistically. This is realized through the shadow fading term in $\mathrm{PL}(f_c, d_{\max})$. For instance, when using the CI path loss model, $\mathrm{PL}(f_c, d_{\max})$ is expressed as

$$\mathrm{PL}(f_c, d_{\max})[\mathrm{dB}] = 32.4 + 10n\log_{10}(d_{\max}) + 20\log_{10}(f_c) + z * \sigma_{\mathrm{SF}} \quad (10)$$

where σ_{SF} represents the shadow fading standard deviation in dB [31], [50].

The coverage distance calculated using Eqs. (9) and (10) are illustrated in Fig. 6, which are the lower bound of the coverage distances since an omnidirectional antenna pattern (i.e., zero gain) is assumed at the RX. Fig. 6 shows that NYUSIM predicts 1.0%–14.1% greater cell radius compared to 3GPP. For example, when there are 256 BS antenna elements, the maximum coverage distance is 281.4 m and 308.3 m predicted by 3GPP and NYUSIM, respectively, where the latter is 9.6% greater than the former. Note that the downlink and uplink may have different link budgets, and in some cases the cell radius may be uplink limited. However, the precise coverage on either the downlink or uplink may vary widely over time. For example, the BS has higher transmitted power than a UE, but it is divided over all users, and the particular locations and power allocations

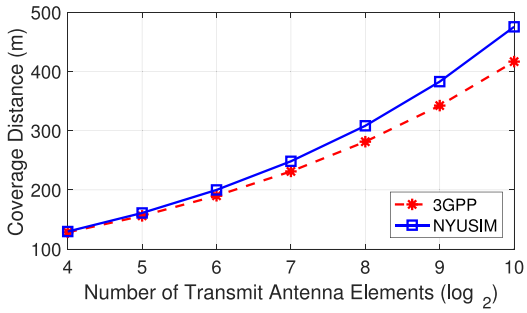

Fig. 6. Maximum coverage distance of the BS as a function of the BS antenna elements in a single-cell three-user MIMO system operating at 28 GHz with an RF bandwidth of 100 MHz in the UMi street canyon scenario, using both 3GPP and NYUSIM channel models.

for beams to different users are dependent on desired sum capacity demands and user applications, and these may impact the particular link state. There is typically more interference margin in the downlink (greater margin exists from the serving cell as compared to outer cell BSs) than in the uplink, where intra-cell interference is more dominant than in the downlink. While the coverage abilities will in general be asymmetric between the downlink and uplink due to different transmit powers, allocations, and interference sources, the cell radius in system design is usually determined from the downlink (not the uplink) and remains unchanged for a BS.[3] As a consequence, for the same T-R separation distance, the uplink received SNR, and hence uplink data rate, will generally be lower than that in the downlink.

B. Antenna Arrays and Architectures

The use of mmWave bands opens up the possibility of using large-scale antenna arrays where hundreds of (if not more) antennas are used. The antenna elements can be arranged in a linear array or a full-dimensional (i.e., with both elevation and azimuth angle resolution capabilities) array. These multi-element antenna arrays will provide spatial multiplexing gain but it is not necessary that an array type in one morphology is best for another. For example, some areas may require elevation beamforming (narrow beams in the elevation) and may need more antennas along the zenith axis as compared to other areas where beamforming in the azimuth may require more antennas in the azimuth. Antenna architectures are also influenced by the horizontal and vertical angle spreads in a multipath channel.

The HBF algorithm proposed in [51] for the fully-connected architecture is employed in this paper to investigate the spectral efficiency in a single-cell SU-MIMO mmWave system, using the simulation settings in Table I with 256 and 16 BS and UE antenna elements, respectively. The CDFs of the spectral efficiency of the single-cell SU-MIMO system are depicted in Fig. 7 for different numbers of RF chains and data streams using both 3GPP [11] and NYUSIM [16] channel models. The number of RF chains in the legend denotes both the transmit and receive

[3]The coverage radius may be uplink limited in some cases, but the example shown here serves to illustrate the differences in cell radii due to channel models. Furthermore, in the case of 5G, there is a 3GPP feature to decouple bands for downlink and uplink, and to enable uplink in the lower microwave band. This will alleviate link budget asymmetries in downlink and uplink.

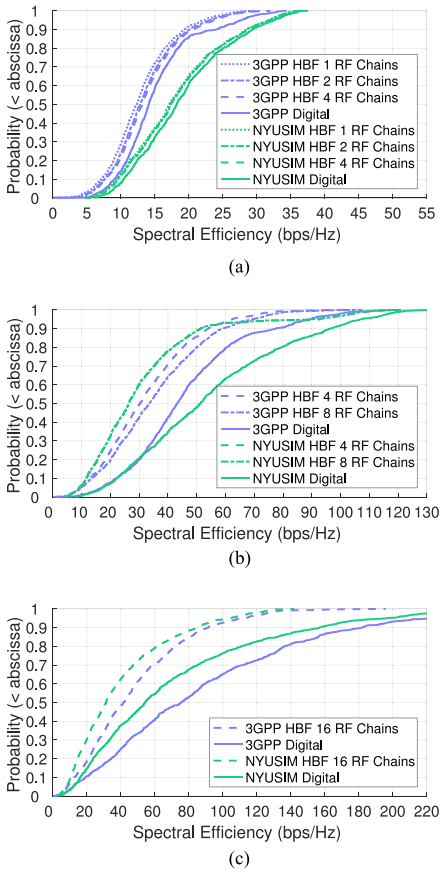

Fig. 7. CDFs of the spectral efficiency of the single-cell SU-MIMO system using the HBF algorithm proposed in [51] for different numbers of RF chains using both 3GPP [11] and NYUSIM [16] channel models. The number of RF chains in the legend denotes both the transmit and receive RF chains. The number of data streams between the BS and UE is one, four, and 16 in (a), (b), and (c), respectively. (a) One Data Stream. (b) Four Data Streams. (c) 16 Data Streams.

RF chains. Fig. 7(a) depicts the case of one data stream, which shows that regardless of the number of RF chains, the spectral efficiency yielded by NYUSIM is larger than that generated by the 3GPP model when only one data stream is transmitted, due to the larger dominant channel eigenvalue produced by NYUSIM. Furthermore, the spectral efficiency using the HBF algorithm is closer to the digital beamforming performance utilizing NYUSIM than using the 3GPP model. More importantly, for the 3GPP model, there is a noticeable increase in the spectral efficiency as the number of RF chains increases from 1 to 4, while the spectral efficiency increase is very trivial for NYUSIM. Fig. 7(b) illustrates the case of four data streams. Several observations can be drawn from Fig. 7(b). First, the digital beamforming spectral efficiency using NYUSIM is larger as compared to the 3GPP channel model in most cases, since the sum of the highest four channel eigenvalues in NYUSIM is greater than that in the 3GPP channel model. Second, for CDF points lower than 90%, the spectral efficiency gap between the digital beamforming and HBF is more significant for NYUSIM than for the 3GPP model, which indicates that the product of the analog and digital hybrid beamforming matrices can not be made sufficiently close to the optimal digital beamforming matrix as required in [51]. This is probably because in some channel realizations the number of MPCs produced by NYUSIM is smaller than four, such that there are not large enough antenna array response vector basis from which the analog steering directions can be selected [51]. Moreover, for the 3GPP channel model, the spectral efficiency increases when the number of RF chains increases from 4 to 8, likely due to the fact that the number of clusters in the UMi scenario in the 3GPP channel model is 12 for LOS and 19 for NLOS, thus increasing the RF chains from 4 to 8 can make better use of the channel spatial dimensions. As a comparison, the spectral efficiency yielded by NYUSIM remains almost unchanged for 4 and 8 RF chains, since the number of spatial lobes does not exceed 5 with an average number of 2 so that increasing the number of RF chains from 4 to 8 is unlikely to provide extra multiplexing gain. Therefore, the 3GPP model suggests that spectral efficiency can be enhanced by increasing the number of RF chains, while NYUSIM indicates that there is no need to increase the RF chains beyond five or so as the spectral efficiency will not be improved. The spectral efficiency CDFs corresponding to 16 data streams and 16 RF chains are displayed in Fig. 7(c), which reveals that the 3GPP model yields higher spectral efficiency for both HBF and digital beamforming. This is because of the increased number of data streams hence increased multipath richness that makes the 3GPP channel closer to a Rayleigh channel, thus resulting in larger spectral efficiency.

Overall, it can be drawn from Fig. 7 that NYUSIM predicts a higher spectral efficiency only when the number of total data streams to a UE is smaller than the channel rank (2–3 on average). Furthermore, the SU-MIMO HBF algorithm in [51] intrinsically assigns dominant paths, instead of weaker paths, to the UE. For any BS-UE pair, there are always dominant paths for that specific UE, thus it is always feasible to send signals on the dominant paths.

The spectral efficiency illustrated in Fig. 7 is obtained under the assumption of full channel state information (CSI) at both the UE and BS. In practical 5G mobile systems, however, acquiring CSI may never be perfect, and requires heavy feedback overhead, especially with large antenna arrays since the channel coefficient for each antenna element has to be estimated. Therefore, it is worth examining the achievable rate using a practical limited feedback HBF scheme, assuming full CSI at the UE and no CSI at the BS, and assuming the UE reports back quantized CSI to the BS via limited feedback. The limited feedback HBF scheme in [51, Sec. V] was adopted to calculate spectral efficiency for the SU-MIMO system in Fig. 7. Specifically, the UE RX quantizes the RF precoder by selecting the antenna array response vectors corresponding to the AoDs and then feeds back the index of the selected angles to the BS TX [51]. The baseband precoder is also quantized at the UE RX via random vector quantization where the chordal distance is used as a distance measure [51], after which the index of the selected baseband precoder is fed back to the BS TX.

The resultant spectral efficiency with the more practical, limited CSI feedback method of [51] is plotted in Fig. 8 as a function of both the number of quantization bits per angle in the RF precoding stage and the number of quantization bits in the baseband precoding stage, respectively, for both 3GPP and NYUSIM channel models. The number of RF chains is four at

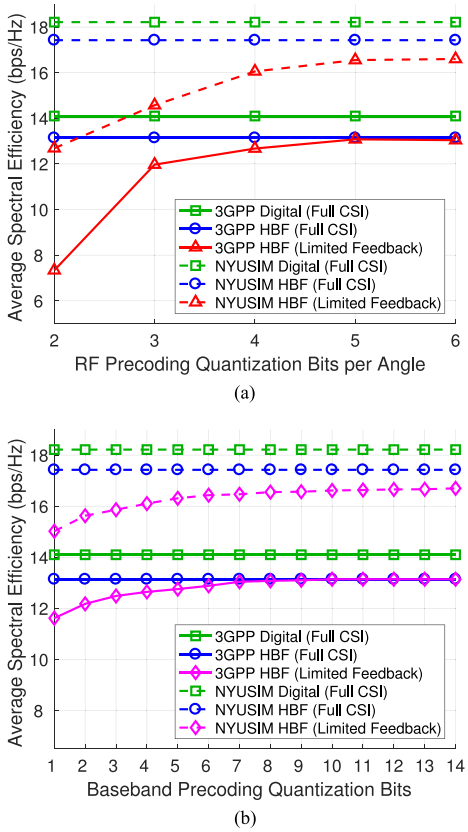

Fig. 8. Average spectral efficiency (averaged over 1000 channel realizations) vs. (a) quantization bits per angle for RF precoding and (b) quantization bits for baseband precoding for the SU-MIMO system using 3GPP and NYUSIM channel models. The number of antenna elements at the BS and UE are 256 and 16, respectively. The number of RF chains is four at both BS and UE, the number of streams is one, and equal quantization bits are assumed for azimuth and elevation angles. The baseband precoder codebook of (a) uses 8 bits. The RF precoder codebook of (b) uses 5 bits.

both BS and UE, the number of streams is one, and an equal and varying number of quantization bits are assumed for azimuth and elevation angles. The spectral efficiency is averaged over 1000 channel realizations. Fig. 8(a) indicates that for the 3GPP model, no more than 5 bits (i.e., quantizing the entire 0°–360° angle range with an angle interval of 11.25°) are needed to quantize each steering angle in the RF precoding stage at the BS to achieve similar performance to the full CSI case. While for NYUSIM, more than 6 bits (i.e., quantizing the entire 0°-360° angle range with an angle interval of 5.625°) are required to converge to the full CSI case, probably due to the higher sparsity level, which means fewer spatial lobes, predicted by NYUSIM as compared to the 3GPP model [11], [38]. Fig. 8(b) shows that 8 bits for the baseband precoding codebook are often enough to achieve comparable performance as compared to the full CSI case using the 3GPP model, and more than 14 bits are needed for NYUSIM. Similar observations are drawn for more than one stream per user (not shown here for brevity).

Table II compares the number of RF chains needed for both 3GPP and NYUSIM channel models to achieve the same or similar spectral efficiency using the HBF algorithm proposed in [51] under the assumption of 28 GHz carrier frequency and 100 MHz

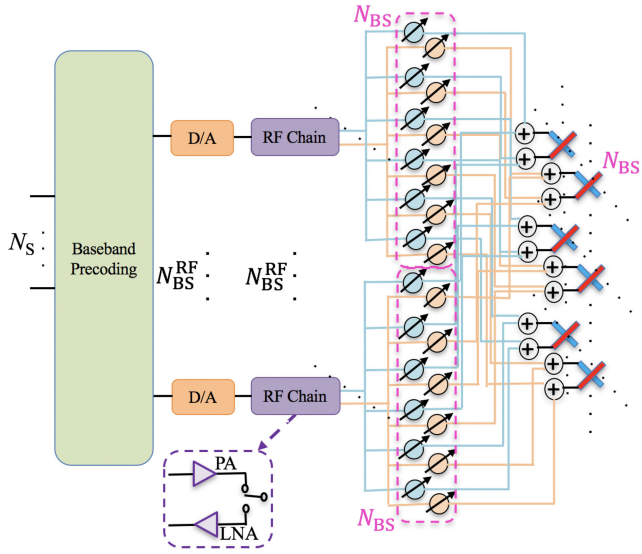

Fig. 9. An example of the HBF architecture diagram with various hardware units at the BS (the MS side can be derived similarly), with N_{BS} antenna elements composing a URA, $N_{\mathrm{BS}}^{\mathrm{RF}}$ RF chains, and N_{S} data streams.

RF bandwidth. Note that for HBF, adding one RF chains entails the addition of one extra DAC/ADC at the BS/MS, one extra power amplifier (PA) and low-noise amplifier (LNA) at the BS/MS, as well as $N_{\mathrm{BS}}/N_{\mathrm{MS}}$ extra phase shifters at the BS/MS, as shown in Fig. 9, which significantly increases the hardware complexity, cost, and power consumption, especially for large N_{BS} and N_{MS} that are likely to be the case in mmWave systems. It is evident from Table II that when the number of data streams is no larger than three, the 3GPP model necessitates more RF chains to achieve comparable spectral efficiency to NYUSIM. For instance, when only one data stream is transmitted, the average spectral efficiency yielded by the 3GPP model even with the maximum possible RF chains (256 TX RF chains and 16 RX RF chains) is still smaller than the NYUSIM spectral efficiency with the minimum possible RF chains (one TX RF chain and one RX RF chain), due to the much stronger dominant eigen channel in NYUSIM as shown in Fig. 4. When two data streams are transmitted, the 3GPP model needs three times as many RF chains and phase shifters to yield similar spectral efficiency to that of NYUSIM. When four or more data streams are transmitted, NYUSIM can generate similar spectral efficiency with comparable or fewer total RF chains as compared to the 3GPP model, but more data streams are required since the third and latter eigen channels in NYUSIM are much weaker than those in the 3GPP model.

C. *Spectral Efficiency Studies*

Whilst the single-cell (with single or multiple users) scenario provides a benchmark for comparison, the multi-cell multi-user case is closer to what is deployed in practice. In this subsection, we investigate the channel spectral efficiency of a multi-cell MU-MIMO system using HBF. It is assumed that in the system there are three adjacent cells with one BS and three UEs per cell. Fig. 10 depicts an example of the three-cell layout. The radius of each cell is 300 m, which is obtained by assuming

TABLE II
RF HARDWARE NEEDED FOR THE 3GPP CHANNEL MODEL [11] AND NYUSIM [16] TO ACHIEVE THE SAME OR SIMILAR SPECTRUM EFFICIENCY IN THE SINGLE-CELL SU-MIMO CASE USING THE HBF ALGORITHM PROPOSED IN [51] FOR THE UMI SCENARIO

Beamforming Approach	Channel Model	Average Spectral Efficiency (bps/Hz)	Number of Streams	Number of TX RF Chains	Number of RX RF Chains	Number of Phase Shifters at TX/RX	Number of PAs/LNAs at TX/RX
Digital	**3GPP**	15.1	1	256	16	256 / 16	256 / 16
	NYUSIM	19.0	1	256	16	256 / 16	256 / 16
HBF	**3GPP**	12.8	1	1	1	256 / 16	1 / 1
	NYUSIM	18.0	1	1	1	256 / 16	1 / 1
	3GPP	22.8	2	6	6	1536 / 96	6 / 6
	NYUSIM	22.9	2	2	2	512 / 32	2 / 2
	3GPP	29.6	3	6	4	1536 / 64	6 / 4
	NYUSIM	29.6	3	3	3	768 / 48	3 / 3
	3GPP	35.2	4	8	4	2048 / 64	8 / 4
	NYUSIM	35.3	5	5	5	1280 / 80	5 / 5

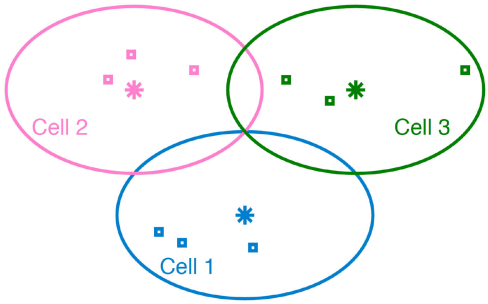

Fig. 10. An example of the three-cell layout where there is one BS and three UEs per cell generated using MATLAB. The radius of each cell is 300 m. The UEs in each cell are distributed uniformly and randomly with T-R separation distances ranging from 10 m to 300 m [11].

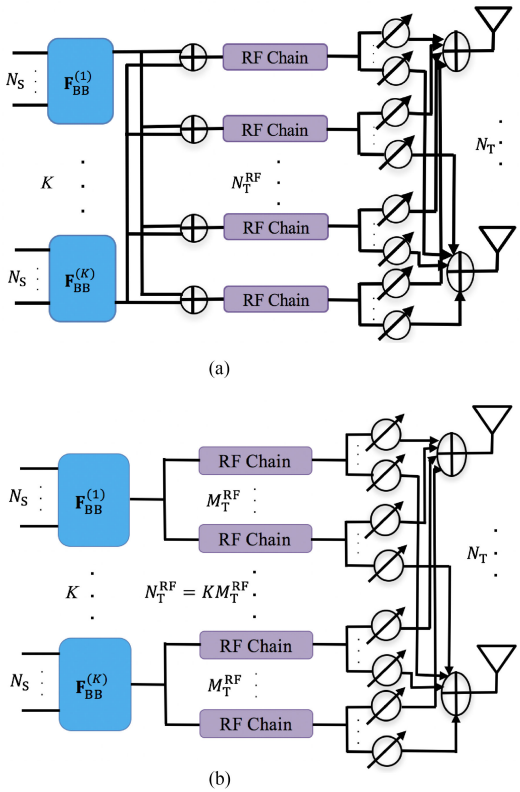

Fig. 11. Two types of multi-cell HBF architectures, FCBP and PCBP, at the BS in each cell. N_{S} denotes the number of data streams per user in each cell, K is the number of users in each cell, $N_{\mathrm{T}}^{\mathrm{RF}}$ represents the total number of RF chains at each BS, $M_{\mathrm{T}}^{\mathrm{RF}}$ is the number of RF chains connected to the baseband precoder for one user in (b), and N_{T} denotes the number of BS antenna elements in each cell. (a) Fully-connected baseband precoders (FCBP). (b) Partially-connected baseband precoders (PCBP).

that 95% of the area in a cell has an SNR larger than or equal to 5 dB, and the upper bound of the T-R separation distance is calculated based on this assumption and rounded to 300 m (see Fig. 6 for 256 BS antenna elements) for both models for fair comparison. The UEs in each cell are distributed uniformly and randomly with T-R separation distances ranging from 10 m to 300 m [11].

Two multi-cell MU-MIMO HBF architectures at each BS are considered in this paper, as illustrated in Fig. 11. For both the structure with fully-connected baseband precoders (FCBP) and the structure with partially-connected baseband precoders (PCBP) in Fig. 11, there is a baseband precoder dedicated to each user, each RF chain is connected to *all* the antenna elements, and the number of RF chains (hence the number of phase shifters) in PCBP can be equal to, larger than, or smaller than those in FCBP. The main difference between FCBP and PCBP is how the baseband precoders for each user are connected to the RF chains. In FCBP, the baseband precoder for a user is connected to all the RF chains, while in PCBP, the baseband precoder for a user is connected to only a subset of RF chains. Let us first focus on the multi-cell MU-MIMO HBF architecture FCBP shown in Fig. 11(a), for which a multi-cell MU-MIMO HBF approach is developed in this paper to calculate the spectral efficiency. Let us consider the three-cell MU-MIMO system illustrated in Fig. 10. Each BS and each user have the same antenna array settings as in the single-cell case. Each BS has $N_{\mathrm{T}}^{\mathrm{RF}}$ RF chains and communicates with each user via N_{S} data streams, and each user has $N_{\mathrm{R}}^{\mathrm{RF}}$ RF chains, with $N_{\mathrm{S}} \leq \min(N_{\mathrm{T}}^{\mathrm{RF}}, N_{\mathrm{R}}^{\mathrm{RF}})$. Analog and digital hybrid beamforming is assumed to be used at both the BS and the user. For BS i (the BS in the ith cell)

$$\begin{aligned}\mathrm{SLNR} &= \frac{\mathbb{E}\left[\frac{P_{\mathrm{t}}}{\eta_{k,l}}\mathbf{s}_{k,l}^H\mathbf{F}_{\mathrm{BB}_{k,l}}^H\breve{\mathbf{H}}_{k,l,l}^H\breve{\mathbf{H}}_{k,l,l}\mathbf{F}_{\mathrm{BB}_{k,l}}\mathbf{s}_{k,l}\right]}{\mathbb{E}\left[\sum_{(m,i)\neq(k,l)}\frac{P_{\mathrm{t}}}{\eta_{k,l}}\mathbf{s}_{k,l}^H\mathbf{F}_{\mathrm{BB}_{k,l}}^H\breve{\mathbf{H}}_{m,i,l}^H\breve{\mathbf{H}}_{m,i,l}\mathbf{F}_{\mathrm{BB}_{k,l}}\mathbf{s}_{k,l}\right]+\mathbb{E}\left[\mathbf{n}_{k,l}^H\mathbf{W}_{\mathrm{RF}_{k,l}}\mathbf{W}_{\mathrm{RF}_{k,l}}^H\mathbf{n}_{k,l}\right]} \\ &= \frac{\mathrm{Tr}\left(\frac{P_{\mathrm{t}}}{\eta_{k,l}}\mathbf{F}_{\mathrm{BB}_{k,l}}^H\breve{\mathbf{H}}_{k,l,l}^H\breve{\mathbf{H}}_{k,l,l}\mathbf{F}_{\mathrm{BB}_{k,l}}\right)}{\mathrm{Tr}\left(\sum_{\substack{(m,i)\\\neq(k,l)}}\frac{P_{\mathrm{t}}}{\eta_{k,l}}\mathbf{F}_{\mathrm{BB}_{k,l}}^H\breve{\mathbf{H}}_{m,i,l}^H\breve{\mathbf{H}}_{m,i,l}\mathbf{F}_{\mathrm{BB}_{k,l}}\right)+N_0\mathrm{Tr}(\mathbf{W}_{\mathrm{RF}_{k,l}}\mathbf{W}_{\mathrm{RF}_{k,l}}^H)} \\ &= \frac{\mathrm{Tr}(\mathbf{F}_{\mathrm{BB}_{k,l}}^H\breve{\mathbf{H}}_{k,l,l}^H\breve{\mathbf{H}}_{k,l,l}\mathbf{F}_{\mathrm{BB}_{k,l}})}{\mathrm{Tr}(\mathbf{F}_{\mathrm{BB}_{k,l}}^H\tilde{\mathbf{H}}_{k,l}^H\tilde{\mathbf{H}}_{k,l}\mathbf{F}_{\mathrm{BB}_{k,l}})+\frac{\eta_{k,l}}{P_{\mathrm{t}}}N_0\mathrm{Tr}(\mathbf{W}_{\mathrm{RF}_{k,l}}\mathbf{W}_{\mathrm{RF}_{k,l}}^H)}\end{aligned} \tag{13}$$

and the kth user in the lth cell, the $N_{\mathrm{R}}\times N_{\mathrm{T}}$ downlink channel is denoted as $\mathbf{H}_{k,l,i}$, the $N_{\mathrm{T}}\times N_{\mathrm{T}}^{\mathrm{RF}}$ RF precoding matrix is $\mathbf{F}_{\mathrm{RF}_i}$, the $N_{\mathrm{T}}^{\mathrm{RF}}\times KN_{\mathrm{S}}$ baseband precoding matrix is $\mathbf{F}_{\mathrm{BB}_i}=[\mathbf{F}_{\mathrm{BB}_{1,i}},...,\mathbf{F}_{\mathrm{BB}_{K,i}}]$ where K denotes the number of users per cell, the $N_{\mathrm{R}}\times N_{\mathrm{R}}^{\mathrm{RF}}$ RF combining matrix and the $N_{\mathrm{R}}^{\mathrm{RF}}\times N_{\mathrm{S}}$ baseband combining matrix is $\mathbf{W}_{\mathrm{RF}_{k,l}}$ and $\mathbf{W}_{\mathrm{BB}_{k,l}}$, respectively. The CSI between a BS and its home-cell user is assumed to be available at both the BS and the user. Coordinated beamforming in CoMP is considered where the CSI, but not the data of users, is shared among all the BSs to enable joint beamforming design, whereas the data of each user is transmitted by its own serving BS. The received signal at the kth user in the lth cell can be formulated as

$$\begin{aligned}\mathbf{y}_{k,l} &= \underbrace{\sqrt{\frac{P_{\mathrm{t}}}{\eta_{k,l}\mathrm{PL}_{k,l,l}}}\mathbf{W}_{\mathrm{BB}_{k,l}}^H\mathbf{W}_{\mathrm{RF}_{k,l}}^H\mathbf{H}_{k,l,l}\mathbf{F}_{\mathrm{RF}_l}\mathbf{F}_{\mathrm{BB}_{k,l}}\mathbf{s}_{k,l}}_{\text{Desired Signal}} \\ &+ \underbrace{\sum_{\substack{(m,i)\\\neq(k,l)}}\sqrt{\frac{P_{\mathrm{t}}}{\eta_{m,i}\mathrm{PL}_{k,l,i}}}\mathbf{W}_{\mathrm{BB}_{k,l}}^H\mathbf{W}_{\mathrm{RF}_{k,l}}^H\mathbf{H}_{k,l,i}\mathbf{F}_{\mathrm{RF}_i}\mathbf{F}_{\mathrm{BB}_{m,i}}\mathbf{s}_{m,i}}_{\text{Interference}} \\ &+ \underbrace{\mathbf{W}_{\mathrm{BB}_{k,l}}^H\mathbf{W}_{\mathrm{RF}_{k,l}}^H\mathbf{n}_{k,l}}_{\text{Noise}}\end{aligned} \tag{11}$$

where P_{t} represents the transmit power for each user in Watts or milli-Watts (mW), $\mathrm{PL}_{k,l,i}$ denotes the large-scale distance-dependent path loss in Watts or mW, including shadow fading, from BS i to user k in cell l, $\eta_{k,l}=||\mathbf{F}_{\mathrm{RF}_l}\mathbf{F}_{\mathrm{BB}_{k,l}}||_F^2$ is a scaling factor to satisfy the per-user transmit power constraint $||\sqrt{P_{\mathrm{t}}}\mathbf{F}_{\mathrm{RF}_l}\mathbf{F}_{\mathrm{BB}_{k,l}}/\sqrt{\eta_{k,l}}||_F^2=P_{\mathrm{t}}$, where F denotes the Frobenius norm. $\mathbf{s}_{k,l}$ represents the desired transmitted signal for user k in cell l with $\mathbb{E}[\mathbf{s}_{k,l}\mathbf{s}_{k,l}^H]=\mathbf{I}_{N_{\mathrm{S}}}$, and $\mathbf{n}_{k,l}\sim\mathcal{CN}(\mathbf{0},N_0\mathbf{I}_{N_{\mathrm{R}}})$ is circularly symmetric complex Gaussian noise with variance N_0.

We intend to maximize the signal-to-interference-plus-noise ratio (SINR) at each user to achieve high spectral efficiency. Directly maximizing the SINR involves a challenging optimization problem with coupled variables, thus the SLNR is utilized as an alternative optimization criterion. Furthermore, the SLNR-based HBF has been proved to yield the highest spectral efficiency and has comparable computational complexity when compared to some other HBF approaches presented and detailed in [28]. The term *leakage* refers to the amount of interference caused by the signal intended for the desired user but received by the remaining users, in contrast to *interference* that is transmitted from undesired BSs and received by the desired user [30]. Take one user in Cell 1 in Fig. 10 as the desired user, for example, the signal transmitted by BS 1 to the desired user is considered as the desired signal, while the signal intended for the desired user but transmitted through links between BS 1 and all the other users is regarded as leakage.

In the SLNR-based HBF, the effective channel matrix $\breve{\mathbf{H}}_{m,i,l}\in\mathbb{C}^{N_{\mathrm{R}}^{\mathrm{RF}}\times N_{\mathrm{T}}^{\mathrm{RF}}}$ is defined as $\frac{1}{\sqrt{\mathrm{PL}_{m,i,l}}}\mathbf{W}_{\mathrm{RF}_{m,i}}^H\mathbf{H}_{m,i,l}\mathbf{F}_{\mathrm{RF}_l}$, and the $(KL-1)N_{\mathrm{R}}^{\mathrm{RF}}\times N_{\mathrm{T}}^{\mathrm{RF}}$ leakage matrix is given by

$$\tilde{\mathbf{H}}_{k,l}=\left[\breve{\mathbf{H}}_{1,1,l}^T,...,\breve{\mathbf{H}}_{k-1,l,l}^T,\breve{\mathbf{H}}_{k+1,l,l}^T,...,\breve{\mathbf{H}}_{K,L,l}^T\right]^T \tag{12}$$

The RF precoding and combining matrices $\mathbf{F}_{\mathrm{RF}_l}$ and $\mathbf{W}_{\mathrm{RF}_{k,l}}$ are designed such that $||\mathbf{W}_{\mathrm{RF}_{k,l}}^H\mathbf{H}_{k,l,l}\mathbf{F}_{\mathrm{RF}_l}||_F^2$ is maximized. The RF beamforming approach in Eqs. (12)–(14) proposed in [52] is applied to obtain $\mathbf{F}_{\mathrm{RF}_l}$ and $\mathbf{W}_{\mathrm{RF}_{k,l}}$, where the codebooks for $\mathbf{F}_{\mathrm{RF}_l}$ and $\mathbf{W}_{\mathrm{RF}_{k,l}}$ consist of the BS and MS antenna array response vectors, respectively [51].

The baseband precoding matrix $\mathbf{F}_{\mathrm{BB}_{k,l}}$ is designed to maximize the SLNR as follows. The expected received signal power prior to the baseband combining process is $\mathbb{E}\left[\frac{P_{\mathrm{t}}}{\eta_{k,l}}\mathbf{s}_{k,l}^H\mathbf{F}_{\mathrm{BB}_{k,l}}^H\breve{\mathbf{H}}_{k,l,l}^H\breve{\mathbf{H}}_{k,l,l}\mathbf{F}_{\mathrm{BB}_{k,l}}\mathbf{s}_{k,l}\right]$, the expected leakage power is $\mathbb{E}\left[\sum_{(m,i)\neq(k,l)}\frac{P_{\mathrm{t}}}{\eta_{k,l}}\mathbf{s}_{k,l}^H\mathbf{F}_{\mathrm{BB}_{k,l}}^H\breve{\mathbf{H}}_{m,i,l}^H\breve{\mathbf{H}}_{m,i,l}\mathbf{F}_{\mathrm{BB}_{k,l}}\mathbf{s}_{k,l}\right]$, and the expected noise power is $\mathbb{E}\left[\mathbf{n}_{k,l}^H\mathbf{W}_{\mathrm{RF}_{k,l}}\mathbf{W}_{\mathrm{RF}_{k,l}}^H\mathbf{n}_{k,l}\right]$. The SLNR is formulated as in (13) shown at the top of this page [30], where N_0 denotes the noise power, and $\tilde{\mathbf{H}}_{k,l}$ is given by (12). The optimal $\mathbf{F}_{\mathrm{BB}_{k,l}}$ that maximizes the SLNR in (13) can be derived similarly to the precoding matrix in [30] and is composed of the leading N_{S} columns of $\mathbf{T}_{k,l}$ which contains the generalized eigenvectors of the pair $\left\{\breve{\mathbf{H}}_{k,l,l}^H\breve{\mathbf{H}}_{k,l,l},\ \tilde{\mathbf{H}}_{k,l}^H\tilde{\mathbf{H}}_{k,l}+\gamma\mathbf{I}_{M_{\mathrm{T}}^{\mathrm{RF}}}\right\}$, where γ satisfies:

$$\mathrm{Tr}(\gamma\mathbf{F}_{\mathrm{BB}_{k,l}}^H\mathbf{F}_{\mathrm{BB}_{k,l}})=\frac{\eta_{k,l}}{P_{\mathrm{t}}}N_0\mathrm{Tr}(\mathbf{W}_{\mathrm{RF}_{k,l}}\mathbf{W}_{\mathrm{RF}_{k,l}}^H) \tag{14}$$

$\mathbf{W}_{\mathrm{BB}_{k,l}}$ is designed as a matched filter at the receiver [30]

$$\mathbf{W}_{\mathrm{BB}_{k,l}}=\frac{\breve{\mathbf{H}}_{k,l,l}\mathbf{F}_{\mathrm{BB}_{k,l}}}{||\breve{\mathbf{H}}_{k,l,l}\mathbf{F}_{\mathrm{BB}_{k,l}}||_F} \tag{15}$$

The spectral efficiency of the kth user in the lth cell is calculated as in (16), shown at the bottom of this page, where P_{t} denotes the transmit power per user, and the interference term $\mathbf{D}$ is given by

$$\mathbf{D} = \sum_{\substack{(m,i)\\ \neq (k,l)}} \frac{P_{\mathrm{t}}}{\eta_{m,i}\mathrm{PL}_{k,l,i}} \mathbf{H}_{k,l,i}\mathbf{F}_{\mathrm{RF}_i}\mathbf{F}_{\mathrm{BB}_{m,i}}\mathbf{F}^H_{\mathrm{BB}_{m,i}}\mathbf{F}^H_{\mathrm{RF}_i}\mathbf{H}^H_{k,l,i} \tag{17}$$

Using the multi-cell MU-MIMO HBF procedure and the three-cell layout illustrated in Fig. 10, and the simulation settings shown in Table I with 256 and 8 antenna elements per BS and UE, respectively, spectral efficiency is studied for both the 3GPP and NYUSIM channel models via MATLAB simulations. It is assumed that there are two RF chains at each UE, and each BS communicates with each UE via two data streams. The number of BS RF chains was varied in the simulations. For each channel model, 200 random channel realizations were carried out where 27 channel matrices were generated in each channel realization (hence resulting in 5400 channel matrices in total), which comprise the channel matrices between each BS and each UE in the three cells. In each channel realization, UE locations are randomly and uniformly generated with T-R separation distances ranging from 10 m to 300 m in each cell [11]. It is also assumed that 95% of the area in each cell has an SNR larger than or equal to 5 dB, and the upper bound of the T-R separation distance is calculated based on this assumption and rounded to 300 m (see Fig. 6 for 256 BS antenna elements) for both models for fair comparison.

The CDFs of the spectral efficiency per user in the three-cell MU-MIMO system using both 3GPP [11] and NYUSIM [16] channel models are plotted in Fig. 12(a), where there are eight RF chains per BS, and two RF chains per UE. Fig. 12(a) shows that the spectral efficiency of individual users produced by NYUSIM varies between 0.002 bps/Hz and 19.6 bps/Hz, and the median values for all the nine users range from 5.4 bps/Hz to 6.2 bps/Hz which are close to each other. While for the 3GPP channel model, the spectral efficiency of individual users ranges from 0.004 bps/Hz to 13.7 bps/Hz, and the median values for all the nine users fall between 2.5 bps/Hz and 3.4 bps/Hz, which are about a half smaller on average as compared to NYUSIM. Fig. 12(b) illustrates the CDFs of the sum spectral efficiency of the nine UEs in the three cells. Fig. 12(b) reveals that for NYUSIM, the sum spectral efficiency ranges from 20.8 bps/Hz to 98.9 bps/Hz with a median value of 57.3 bps/Hz. On the other hand, for the 3GPP channel model, the sum spectral efficiency varies between 11.2 bps/Hz and 61.3 bps/Hz with a median value of 32.7 bps/Hz which is 42.9% smaller than the median value yielded by NYUSIM.

As a comparison, Fig. 13 illustrates the per-user and sum spectral efficiencies for the case of 20 RF chains per BS and two RF chains per UE. It is evident from Fig. 13 that the spectral efficiencies generated by the 3GPP channel model increase significantly when the number of RF chains per BS grows from eight to 20. For instance, the median value of the per-user spectral efficiency for the case of 20 RF chains per BS varies from 3.4 to 5.1 bps/Hz as shown by Fig. 13(a), and the median value of the sum spectral efficiency becomes 44.3 bps/Hz as shown by Fig. 13(b), which is 11.6 bps/Hz larger than that in Fig. 12(b) for the eight RF chains per BS case.

Using a similar algorithm as shown in Eqs. (11) - (17) for the HBF architecture depicted in Fig. 11(b), we compute the sum spectral efficiency and compare it with that for the HBF architecture in Fig. 11(a) for $K = 3$, $N_{\mathrm{S}} = 2$, and $N_{\mathrm{T}}^{\mathrm{RF}} = 6$, and show the 10%, 50%, and 90% CDF points in Table III. It is observed from Table III that for both 3GPP and NYUSIM

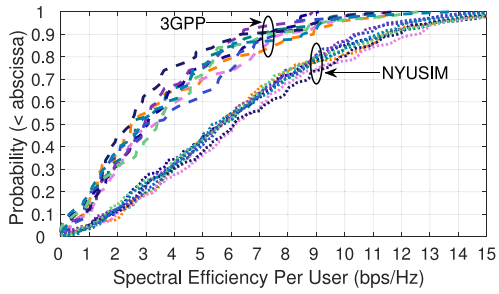

(a)

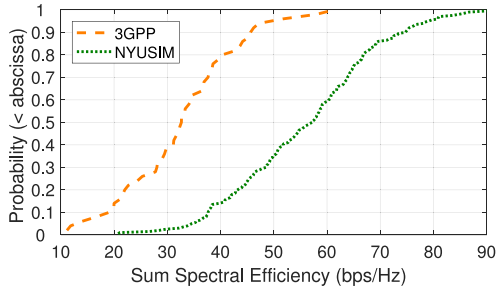

(b)

Fig. 12. CDFs of the (a) per-user spectral efficiency (Eight RF chains) and (b) sum spectral efficiency (Eight RF chains) of the three-cell MU-MIMO system using the SLNR-based HBF approach proposed in this paper for 3GPP [11] and NYUSIM [16] channel models. There is one BS and three UEs per cell, and the radius of each cell is 300 m.

TABLE III
SUM SPECTRAL EFFICIENCY IN BPS/HZ IN MULTI-CELL MULTI-USER MIMO SYSTEMS FOR BOTH TYPES OF BASE STATION HBF ARCHITECTURE SHOWN IN FIG. 11 USING 3GPP [11] AND NYUSIM [16], [38] CHANNEL MODELS

	Sum Spectral Efficiency (bps/Hz)	10% Point	50% Point	90% Point
Structure 1 (Fig. 11(a))	3GPP	14.0	29.5	41.0
	NYUSIM	38.1	56.9	79.0
Structure 2 (Fig. 11(b))	3GPP	27.1	52.1	65.3
	NYUSIM	56.9	77.3	98.1

$$R_{k,l} = \log_2\left|\mathbf{I}_{N_{\mathrm{S}}} + \frac{P_{\mathrm{t}}}{\eta_{k,l}\mathrm{PL}_{k,l,l}}\left(\mathbf{W}^H_{\mathrm{BB}_{k,l}}\mathbf{W}^H_{\mathrm{RF}_{k,l}}(N_0\mathbf{I}_{N_{\mathrm{R}}} + \mathbf{D})\mathbf{W}_{\mathrm{RF}_{k,l}}\mathbf{W}_{\mathrm{BB}_{k,l}}\right)^{-1}\mathbf{W}^H_{\mathrm{BB}_{k,l}}\breve{\mathbf{H}}_{k,l,l}\mathbf{F}_{\mathrm{BB}_{k,l}}\mathbf{F}^H_{\mathrm{BB}_{k,l}}\breve{\mathbf{H}}^H_{k,l,l}\mathbf{W}_{\mathrm{BB}_{k,l}}\right| \tag{16}$$

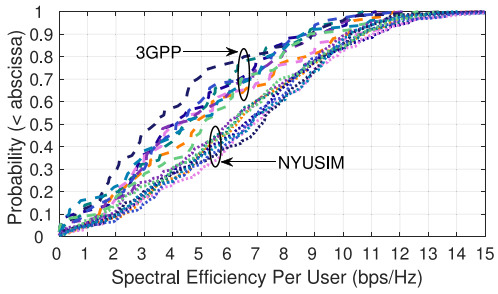

(a)

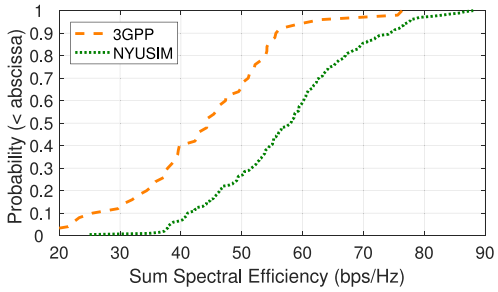

(b)

Fig. 13. CDFs of the (a) per-user spectral efficiency (20 RF chains) and (b) sum spectral efficiency (20 RF chains) of the three-cell MU-MIMO system using the SLNR-based HBF approach proposed in this paper for 3GPP [11] and NYUSIM [16] channel models. There is one BS and three UEs per cell, and the radius of each cell is 300 m.

models, the HBF architecture in Fig. 11(b) produces higher spectral efficiency, most likely due to the fact that each RF chain is shared over fewer streams such that the interference between streams is lower.

Two major observations are obtained from the simulation results in Figs. 12 and 13, and Table III:

1) For the three-cell MU-MIMO using the SLNR-based HBF approach proposed in this paper with two streams per user, NYUSIM predicts larger per-user and sum spectral efficiencies than the 3GPP channel model, probably because of the stronger two dominant eigen channels per user, and the smaller AoA spread per user such that channels among different users are less correlated leading to less interference when compared to the 3GPP model, as detailed later in Section VI-B.
2) When using the 3GPP channel model, the predicted spectral efficiency increases substantially when the number of RF chains per BS increases from eight to 20, due to the large number of clusters (12 and 19 for UMi LOS and NLOS, respectively) in the 3GPP channel model.

VI. Mathematical Fundamentals: Linking Channel Models to Performance

A. SU-MIMO Capacity

When ignoring antenna patterns, assuming a single polarization and setting the time index to zero, the channel equation for a SU-MIMO system can be expressed as

$$\mathbf{H} = \sum_{i=1}^{L} a_i \mathbf{a}_{\mathrm{R}}(\phi_{\mathrm{R},i}, \theta_{\mathrm{R},i}) \mathbf{a}_{\mathrm{T}}^{H}(\phi_{\mathrm{T},i}, \theta_{\mathrm{T},i}), \tag{18}$$

where L denotes the total number of subpaths/rays in all clusters, a_i is the complex amplitude of the i-th path, $\phi_{\mathrm{R},i}, \theta_{\mathrm{R},i}$ represent azimuth and elevation angles for the i-th AoA, $\phi_{\mathrm{T},i}, \theta_{\mathrm{T},i}$ represent azimuth and elevation angles for the i-th AoD and $\mathbf{a}_{\mathrm{R}}$, $\mathbf{a}_{\mathrm{T}}$ are AoA and AoD steering vectors with unit magnitude elements. Stacking and normalizing the steering vectors into matrices gives $\mathbf{A}_{\mathrm{R}}$ with i-th column, $\mathbf{a}_{\mathrm{R}}(\phi_{\mathrm{R},i}, \theta_{\mathrm{R},i})/\sqrt{N_{\mathrm{R}}}$ and $\mathbf{A}_{\mathrm{T}}$ with i-th column, $\mathbf{a}_{\mathrm{T}}(\phi_{\mathrm{T},i}, \theta_{\mathrm{T},i})/\sqrt{N_{\mathrm{T}}}$. With this notation, the channel matrix can be written as

$$\mathbf{H} = \sqrt{N_{\mathrm{R}} N_{\mathrm{T}}} \mathbf{A}_{\mathrm{R}} \mathbf{D}_a \mathbf{A}_{\mathrm{T}}^{H}, \tag{19}$$

where $\mathbf{D}_a = \mathrm{diag}(a_1, a_2, \ldots, a_L)$. Using the representation in (19), a simple, well-known lower bound for the channel capacity, which becomes tight at high SNR or for peak capacity values, can be written as

$$\begin{aligned} C &= \log_2|\mathbf{I}_{N_{\mathrm{R}}} + \rho \mathbf{H}\mathbf{H}^{H}| \qquad (20)\\ &= \log_2|\mathbf{I}_{N_{\mathrm{R}}} + \rho N_{\mathrm{R}} N_{\mathrm{T}} \mathbf{A}_{\mathrm{R}} \mathbf{D}_a \mathbf{A}_{\mathrm{T}}^{H} \mathbf{A}_{\mathrm{T}} \mathbf{D}_a^{H} \mathbf{A}_{\mathrm{R}}^{H}|\\ &\geq \log_2|\rho N_{\mathrm{R}} N_{\mathrm{T}} \mathbf{D}_a \mathbf{A}_{\mathrm{T}}^{H} \mathbf{A}_{\mathrm{T}} \mathbf{D}_a^{H} \mathbf{A}_{\mathrm{R}}^{H} \mathbf{A}_{\mathrm{R}}|\\ &= L\log_2(\rho N_{\mathrm{R}} N_{\mathrm{T}}) + \sum_{i=1}^{L} \log_2|a_i|^2 + \log_2|\mathbf{R}_{\mathrm{R}}| + \log_2|\mathbf{R}_{\mathrm{T}}|\\ &= T_1 + T_2 + T_3 + T_4, \qquad (21) \end{aligned}$$

where ρ is the SNR at the RX, $\mathbf{R}_x = \mathbf{A}_x^{H}\mathbf{A}_x$ is defined by $(\mathbf{R}_x)_{r,s} = \mathbf{a}_x(\phi_{x,r}, \theta_{x,r})^{H}\mathbf{a}_x(\phi_{x,s}, \theta_{x,s})/N_x$ where $x \in \{\mathrm{R}, \mathrm{T}\}$ and (21) is valid for the sparse case where $L \leq \min\{N_{\mathrm{R}}, N_{\mathrm{T}}\}$. Although (21) is a very simple bound, it has the benefit of clearly demonstrating in closed form the importance of various channel parameters. Some key conclusions following directly from (21) are given below:

- For sparse channels, $L \leq \min\{N_{\mathrm{R}}, N_{\mathrm{T}}\}$, the leading term in the capacity, T_1, grows linearly with L, the number of paths, rather than the array dimension. Hence, performance is limited by L in the sparse domain and models which generate more paths will lead to much higher predicted capacity.
- The second term, T_2, is usually negative and is non-linear in L as the mean of $|a_i|^2$ is inversely proportional to L. The key impact is that smaller path powers cause a larger capacity penalty. This is a similar effect to T_1 as a vanishing path power is equivalent to losing the path. Hence, channel models which spread path powers more evenly will lead to a higher predicted capacity.
- The third and fourth terms, T_3 and T_4, are functions of the steering vectors. They play an equivalent role to spatial correlation matrices in reducing the predicted capacity. This is because the matrices $\mathbf{R}_{\mathrm{R}}$ and $\mathbf{R}_{\mathrm{T}}$ have a leading diagonal containing ones, they are Hermitian and the off diagonals are cross-products of normalized steering vectors. If the steering vectors are all orthogonal at both ends of the link, then $|\mathbf{R}_{\mathrm{R}}| = |\mathbf{R}_{\mathrm{T}}| = 1$ and $T_3 = T_4 = 0$. At the other extreme, if two AoAs or two AoDs converge to each other then $|\mathbf{R}_{\mathrm{R}}|$ and $|\mathbf{R}_{\mathrm{T}}|$ converge to zero as the matrices are not full rank with any equal angles. The $\log_2|\cdot|$ terms in T_3 and T_4 therefore produce a substantial capacity penalty. Clearly, channel models which produce similar ray directions will reduce capacity, e.g. models with a narrow intra

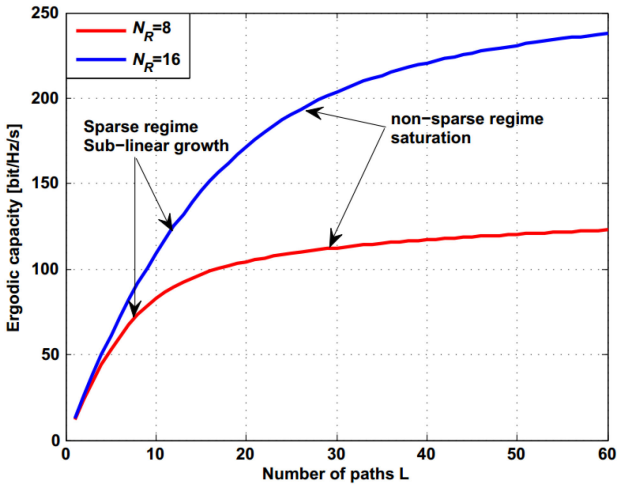

Fig. 14. Ergodic capacity for a SU-MIMO system vs the number of paths for $N_{\mathrm{R}} \in \{8, 16\}$, $N_{\mathrm{T}} = 100$ and $\rho = 10$ dB.

or inter cluster AS or, for a fixed AS, models with a sharper angular distribution, such as the Laplacian.

These conclusions are for the sparse regime, $L \leq \min\{N_{\mathrm{R}}, N_{\mathrm{T}}\}$, where we can see a linear capacity growth in L due to term T_1, offset by the effects of small path powers (T_2) and limited angular spread (T_3 and T_4). For small values of L, there are fewer opportunities for the capacity reduction effects and growth is nearly linear. Across the whole region, the linear term, T_1, remains and reasonable capacity growth with L is expected. In contrast, the non-sparse regime $L > \min\{N_{\mathrm{R}}, N_{\mathrm{T}}\}$ leads to very different conclusions. The channel in (18) becomes Gaussian by the central limit theorem as L grows, with a covariance structure governed by the steering vectors. As L grows, the covariance structure will also stabilize towards the ensemble average predicted by the angular distributions and capacity will converge.

Essentially we have two very different regimes: the sparse regime where capacity has a sub-linear growth and the large-L regime where capacity saturates. This is shown by plotting ergodic capacity ($E(C)$ where C is given in (20)) against the number of paths in Fig. 14 for two system sizes, $(N_{\mathrm{R}}, N_{\mathrm{T}}) = (8, 100)$ and $(N_{\mathrm{R}}, N_{\mathrm{T}}) = (16, 100)$. In both cases we consider a ULA at both ends of the link with uniform ($U[0, 2\pi]$) AoAs and AoDs. The path powers are generated as $a_i \sim CN(0, 1/L)$ and $\rho = 10$dB. The two different regimes are clearly shown in Fig. 14 where each ergodic capacity value is computed from Monte Carlo simulation using 10^4 samples of (20). In terms of channel models, the number of paths is critical and models which give a non-negligible probability of the sparse regime will predict a much lower capacity than models which are dominated by the non-sparse region.

B. MU-MIMO Signal Processing

In the MU-MIMO case the separation of users by various signal processing schemes is critical and it is useful to consider the impact of channel models on particular processing techniques. In this section, we briefly discuss matched filtering (MF) at both transmit and receive ends. As in Section VI-A, the motivation for considering this scheme is simplicity and the ability to gain insight into the effects of channel models.

Consider a downlink channel with K multi-antenna users. The TX uses precoders, $\mathbf{F}_1, \mathbf{F}_2, \ldots, \mathbf{F}_K$, to send the signal vectors, $\mathbf{s}_1, \mathbf{s}_2, \ldots, \mathbf{s}_K$, down the channels, $\mathbf{H}_1, \mathbf{H}_2, \ldots, \mathbf{H}_K$ to the K users. Note that $\mathbf{F}_k = \mathbf{F}_{\mathrm{RF}}\mathbf{F}_{\mathrm{BB}_k}$ is the full precoder comprising both analog and digital components. If user 1 employs the receive combiner $\mathbf{W}_1 = \mathbf{W}_{\mathrm{RF}_1}\mathbf{W}_{\mathrm{BB}_1}$, then the received signal at user 1 after combining is

$$\mathbf{r}_1 = \mathbf{W}_1^H \left(\mathbf{H}_1 \sum_{k=1}^{K} \mathbf{F}_k \mathbf{s}_k + \mathbf{n}_1 \right), \tag{22}$$

where $\mathbf{n}_1$ is additive white Gaussian noise with variance σ^2. Replacing $\mathbf{H}_1$ in (22) by the channel model in (18), the signal carrying component of (22) has power

$$P_{\mathrm{sig}} = \left|\left| \mathbf{W}_1^H \left(\sum_{l=1}^{L} a_l \mathbf{a}_{\mathrm{R}}(\phi_{\mathrm{R},l}, \theta_{\mathrm{R},l}) \mathbf{a}_{\mathrm{T}}^H(\phi_{\mathrm{T},l}, \theta_{\mathrm{T},l}) \right) \mathbf{F}_1 \right|\right|^2, \tag{23}$$

and the other-user interference power is

$$P_{\mathrm{int}} = \sum_{k=2}^{K} \left|\left| \mathbf{W}_1^H \left(\sum_{l=1}^{L} a_l \mathbf{a}_{\mathrm{R}}(\phi_{\mathrm{R},l}, \theta_{\mathrm{R},l}) \mathbf{a}_{\mathrm{T}}^H(\phi_{\mathrm{T},l}, \theta_{\mathrm{T},l}) \right) \mathbf{F}_k \right|\right|^2. \tag{24}$$

The relationship between P_{sig} and the channel parameters is very different to that in Section VI-A. Consider MF performed with limited RF chains, so that $\mathbf{W}_1$ and $\mathbf{F}_1$ rely heavily on analog processing to match the channel. If L is small or if the path powers have a large spread then the channel is dominated by a few steering vectors which, from the inspection of (23), can be extremely well matched by the simple approach of choosing the columns of the analog components of $\mathbf{W}_1$ and $\mathbf{F}_1$ to be the dominant steering vectors. Hence, a sparse channel and highly variable path powers can be an enabler for these processing methods, the opposite conclusion to SU capacity. Also, a wide AS for a given user may not be advantageous, since if only a small number of streams are used for transmission then only a limited number of paths are needed, which need to be separated from each other but not by large angular distances. This is seen clearly in the results of Section V-C, where the RF processing matrices at both ends simply select the best steering vectors and only two streams are used. With such an architecture, channels which put the majority of power in a few directions will give better signal power, so that fewer paths or more variable path powers are advantageous leading to the higher predicted performance of the NYUSIM model. This is also shown in the SU-MIMO case in Figs. 4 and 7. In Fig. 4 we see that the NYUSIM model places far more power in the first two eigen channels than the 3GPP model. As a result, in Fig. 7, spectral efficiency for small numbers of RF chains and a single stream is higher for the NYUSIM model. In contrast, as the number of RF chains and streams grows, more diversity and spatial multiplexing can be used and the 3GPP model predicts better performance.

In terms of interference, the MF approach relies on large numbers of antennas and user diversity to manage the value of P_{int}. As can be seen in (24), ideally the precoders $\mathbf{F}_i$ are orthogonal to the transmit steering vectors of user 1. This is easier if the angular range of steering vectors for user 1 is small,

TABLE IV
SUMMARY OF THE EVALUATION PERFORMANCE ON SPECTRAL EFFICIENCY/CAPACITY OF THE 3GPP CHANNEL MODEL [11] AND NYUSIM [16]

Scenario	Model Predicting Larger Capacity
Spatial Multiplexing Based on H	**3GPP** (due to increased multipath richness in the 3GPP model)
Spatial Multiplexing Based on $\mathbf{HF}_{\mathrm{RF}}$	**3GPP** (due to increased multipath richness in the 3GPP model although $\mathbf{F}_{\mathrm{RF}}$ makes the channel correlated; shown by Fig. 14)
Digital Beamforming	**3GPP (with a large number of data streams) or NYUSIM (with a small number of data streams)** (shown by Fig. 7)
HBF for Single-Cell Single-User Single-Stream	**NYUSIM** (due to channel sparsity and larger dominant eigenvalue in the NYUSIM model and HBF processing that changes the channel properties as seen by the RX; shown by Fig. 7(a))
HBF for Multi-Cell Multi-User Multi-Stream	**NYUSIM** (due to channel sparsity and larger dominant eigenvalue in the NYUSIM model and HBF processing that changes the channel properties as seen by the RX; shown by Figs. 12 and 13)

reinforcing the above comment that a wide AS for a given user may not be advantageous. Also, it is easier if the users have a wide angular separation so that $\mathbf{F}_i$ may be well separated from the transmit steering vectors of user 1. Again, these trends are highly relevant to the scheme in Section V-C, where the RF processors directly use steering vectors of the users. Hence, wide separation of steering vectors between users is useful, which is helped by a restricted number of powerful angular directions for each user. Therefore, sparser channels are advantageous and again, we see the higher predicted performance of the NYUSIM model in Section V-C.

Overall we see that only the benefits of a large inter-user angular separation are found for both SU capacity and for MU MF. For the other channel parameters considered, intra-user spread, path powers and sparsity, the trends are opposite. A numerical example of this is the SLNR based HBF scheme given in Section V-C. In conclusion, not only are the variation of channel parameters critical to performance, their impact varies according to the performance metric of interest. Hence, performance trends can be difficult to extrapolate from one model to another and accurate model choices are doubly important. Based on all the observations on channel spectral efficiency/capacity presented above, we summarize the evaluation performance of the 3GPP and NYUSIM channel models for various spatial multiplexing and beamforming scenarios, which is given in Table IV.

VII. CONCLUSION

This paper provided a comprehensive overview of the channel models for the design of 5G radio systems, including the general framework of channel models and key differences between mmWave and microwave channel models. We compared two representative channel models, the 3GPP model and the NYUSIM model, and demonstrated the profound impact of the models on 5G channel performance evaluation via simulations, including multi-cell multi-user CoMP transmission simulations using promising hybrid beamforming methods. Analyses and simulation results show that channel model selection has a huge influence on deployment decisions and on various channel performance metrics, such as spectrum efficiency, coverage, and hardware/signal processing requirements.

The 3GPP and NYUSIM channel models utilize different LOS probability models, path loss models, cluster definitions, and large-scale and small-scale parameters, etc. Particularly, the number of clusters in the 3GPP model is over two to four times as large as the maximum number of spatial lobes in NYUSIM, leading to different channel sparsity levels in the two models. The difference in LOS probability and path loss models gives rise to discrepant cell radius prediction results that can differ by 50 m or so for around 500 transmit antenna elements. Compared to NYUSIM, the larger cluster number (i.e., more rich multipath) in the 3GPP model results in more eigen channels and more similar powers among those eigen channels, thus is advantageous for spatial multiplexing. On the other hand, the NYUSIM channel exhibits sparsity and has fewer but stronger dominant eigenmodes, hence generating higher spectral efficiency when combined with appropriate HBF procedures. For example, for the one-stream case in a SU-MIMO system using the HBF algorithm in [51], the average spectral efficiency yielded by the 3GPP model even with the maximum possible RF chains is still smaller than the NYUSIM spectral efficiency with the minimum possible RF chains. Different channel models can lead to substantially varied predictions on diverse channel performance metrics and hardware requirements, thus it is vital to select an accurate channel model for 5G wireless system performance evaluation.

REFERENCES

[1] J. Medbo *et al.*, "Radio propagation modeling for 5G mobile and wireless communications," *IEEE Commun. Mag.*, vol. 54, no. 6, pp. 144–151, Jun. 2016.
[2] White paper, "Cisco visual network index: Global mobile traffic forecast update," Cisco, Tech. Rep. 20162021, Mar. 2017.
[3] S. Hur, T. Kim, D. J. Love, J. V. Krogmeier, T. A. Thomas, and A. Ghosh, "Millimeter wave beamforming for wireless backhaul and access in small cell networks," *IEEE Trans. Commun.*, vol. 61, no. 10, pp. 4391–4403, Oct. 2013.
[4] T. L. Marzetta, "Noncooperative cellular wireless with unlimited numbers of base station antennas," *IEEE Trans. Wireless Commun.*, vol. 9, no. 11, pp. 3590–3600, Nov. 2010.
[5] W. Roh *et al.*, "Millimeter-wave beamforming as an enabling technology for 5G cellular communications: Theoretical feasibility and prototype results," *IEEE Commun. Mag.*, vol. 52, no. 2, pp. 106–113, Feb. 2014.
[6] J. G. Andrews, X. Zhang, G. D. Durgin, and A. K. Gupta, "Are we approaching the fundamental limits of wireless network densification?" *IEEE Commun. Mag.*, vol. 54, no. 10, pp. 184–190, Oct. 2016.
[7] M. Shafi *et al.*, "5G: A tutorial overview of standards, trials, challenges, deployment, and practice," *IEEE J. Sel. Areas Commun.*, vol. 35, no. 6, pp. 1201–1221, Jun. 2017.
[8] ITU-R, "Guidelines for evaluation of radio interface technologies for IMT-2020," Int. Telecommun. Union, Geneva, Switzerland, Tech. Rep. M.2412-0, Oct. 2017.
[9] S. Rangan, T. S. Rappaport, and E. Erkip, "Millimeter-wave cellular wireless networks: Potentials & challenges," *Proc. IEEE.*, vol. 102, no. 3, pp. 366–385, Mar. 2014.
[10] 3GPP, "Technical specification group radio access network; Study on 3D channel model for LTE (Release 12)," , 3rd Gener. Partnership Project, Tech. Rep. 36.873 V12.2.0, Jun. 2015.
[11] 3GPP, "Study on channel model for frequencies from 0.5 to 100 GHz," 3rd Gener. Partnership Project, Tech. Rep. 38.901 V14.3.0, Dec. 2017.

[12] *Guidelines for Evaluation of Radio Transmission Technologies for IMT-2000*," Int. Telecommun. Union, Geneva, Switzerland, ITU-R M.1225, 1997.
[13] METIS, "Project management plan," Tech. Rep. D1.2, Mar. 2013.
[14] White Paper, "5G channel model for bands up to 100 GHz," 4th Int. Workshop on 5G/5G+ Communications in Higher Frequency Bands, Oct. 2016. [Online]. Available: http://www.5gworkshops.com/5GCM.html
[15] S. Jaeckel, L. Raschkowski, K. Börner, and L. Thiele, "QuaDRiGa: A 3-D multi-cell channel model with time evolution for enabling virtual field trials," *IEEE Trans. Antennas Propag.*, vol. 62, no. 6, pp. 3242–3256, Jun. 2014.
[16] S. Sun, G. Maccartney, and T. S. Rappaport, "A novel millimeter-wave channel simulator and applications for 5G wireless communications," in *Proc. IEEE Int. Conf. Commun.*, May 2017, pp. 1–7.
[17] A. Maltsev *et al.*, "Channel modeling in the next generation mmWave Wi-Fi: IEEE 802.11ay standard," in *Proc. 22th Eur. Wireless Conf. Eur. Wireless.*, May 2016, pp. 1–8.
[18] A. Fricke *et al.*, "TG3d Channel Modelling Document (CMD)," , IEEE P802.15 Working Group for Wireless Personal Area Networks, Tech. Rep. 15-14-0310-19-003d, Mar. 2016.
[19] K. Hiraga *et al.*, "TG3e channel modelling document (CMD)," IEEE P802.15 Working Group for Wireless Personal Area Networks, Tech. Rep. 15-15-0279-02-003e, May 2015.
[20] R. J. Weiler *et al.*, "Quasi-deterministic millimeter-wave channel models in MiWEBA," *EURASIP J. Wireless Commun. Netw.*, vol. 2016, 2016, Art no 84.
[21] mmMAGIC, "Measurement campaigns and initial channel models for preferred suitable frequency ranges," , 5GPPP, Eurescom GmbH, Heidelberg Germany, Tech. Rep. H2020-ICT-671650-mmMAGIC/D2.1, Mar. 2016. [Online]. Available: https://5g-ppp.eu/mmmagic/
[22] K. Haneda *et al.*, "5G 3GPP-like channel models for outdoor urban microcellular and macrocellular environments," in *Proc. IEEE 83rd Veh. Technol. Conf.*, May 2016, pp. 1–7.
[23] Q. Li *et al.*, "Validation of a geometry-based statistical mmwave channel model using ray-tracing simulation," in *Proc. IEEE 81st Veh. Technol. Conf.*, May 2015, pp. 1–5.
[24] K. Guan *et al.*, "On millimeter wave and THz mobile radio channel for smart rail mobility," *IEEE Trans. Veh. Technol.*, vol. 66, no. 7, pp. 5658–5674, Jul. 2017.
[25] R. He, B. Ai, G. L. Stüber, G. Wang, and Z. Zhong, "Geometrical based modeling for millimeter wave MIMO mobile-to-mobile channels," *IEEE Trans. Veh. Technol.*, vol. 67, no. 4, pp. 2848–2863, Apr. 2018.
[26] T. S. Rappaport, G. R. MacCartney, M. K. Samimi, and S. Sun, "Wideband millimeter-wave propagation measurements and channel models for future wireless communication system design (Invited Paper)," *IEEE Trans. Commun.*, vol. 63, no. 9, pp. 3029–3056, Sep. 2015.
[27] *Guidelines for Evaluation of Radio Interface Technologies for IMT-Advanced*, Int. Telecommun. Union, Geneva, Switzerland, ITU-R M. 2135, 2008.
[28] S. Sun, T. S. Rappaport, and M. Shafi, "Hybrid beamforming for 5G millimeter-wave multi-cell networks," in *Proc. IEEE Conf. Comput. Commun. Workshops*, 2018, pp. 589–596.
[29] T. S. Rappaport *et al.*, "Millimeter wave mobile communications for 5G cellular: It will work!" *IEEE Access*, vol. 1, pp. 335–349, 2013.
[30] M. Sadek, A. Tarighat, and A. H. Sayed, "A leakage-based precoding scheme for downlink multi-user MIMO channels," *IEEE Trans. Wireless Commun.*, vol. 6, no. 5, pp. 1711–1721, May 2007.
[31] T. S. Rappaport *et al.*, *Millimeter Wave Wireless Communications*. Upper Saddle River, NJ, USA: Prentice-Hall, 2015.
[32] T. A. Thomas *et al.*, "A prediction study of path loss models from 2-73.5 GHz in an urban-macro environment," in *Proc. IEEE 83rd Veh. Technol. Conf.*, May 2016, pp. 1–5.
[33] S. Sun *et al.*, "Investigation of prediction accuracy, sensitivity, and parameter stability of large-scale propagation path loss models for 5G wireless communications," *IEEE Trans. Veh. Technol.*, vol. 65, no. 5, pp. 2843–2860, May 2016.
[34] A. F. Molisch and F. Tufvesson, "Propagation channel models for next-generation wireless communications systems," *IEICE Trans. Commun.*, vol. 97, no. 10, pp. 2022–2034, 2014.
[35] ITU-R, "Attenuation by atmospheric gases," Int. Telecommun. Union, Geneva, Switzerland, Tech. Rep. P.676-8, 2009.
[36] H. Zhao *et al.*, "28 GHz millimeter wave cellular communication measurements for reflection and penetration loss in and around buildings in New York city," in *Proc. IEEE Int. Conf. Commun.*, Jun. 2013, pp. 5163–5167.
[37] M. R. Akdeniz *et al.*, "Millimeter wave channel modeling and cellular capacity evaluation," *IEEE J. Sel. Areas Commun.*, vol. 32, no. 6, pp. 1164–1179, Jun. 2014.
[38] M. K. Samimi and T. S. Rappaport, "3-D millimeter-wave statistical channel model for 5G wireless system design," *IEEE Trans. Microw. Theory Techn.*, vol. 64, no. 7, pp. 2207–2225, Jul. 2016.
[39] *Framework and Overall Objectives of the Future Development of IMT for 2020 and Beyond*, Draft New Recommendation ITU, ITU-R M.2083, 2015.
[40] S. Han, C.-I. I, Z. Xu, and C. Rowell, "Large-scale antenna systems with hybrid analog and digital beamforming for millimeter wave 5G," *IEEE Commun. Mag.*, vol. 53, no. 1, pp. 186–194, Jan. 2015.
[41] Y. Tan, C.-X. Wang, J. Ø. Nielsen, and G. F. Pedersen, "Comparison of stationarity regions for wireless channels from 2 GHz to 30 GHz," in *Proc. 13th Int. Wireless Commun. Mobile Comput. Conf.*, Jun. 2017, pp. 647–652.
[42] T. S. Rappaport, G. R. MacCartney, S. Sun, H. Yan, and S. Deng, "Small-scale, local area, and transitional millimeter wave propagation for 5G communications," *IEEE Trans. Antennas Propag.*, vol. 65, no. 12, pp. 6474–6490, Dec. 2017.
[43] X. Yin, C. Ling, and M.-D. Kim, "Experimental multipath-cluster characteristics of 28-GHz propagation channel," *IEEE Access*, vol. 3, pp. 3138–3150, 2015.
[44] M. K. Samimi and T. S. Rappaport, "Local multipath model parameters for generating 5G millimeter-wave 3GPP-like channel impulse response," in *Proc. 10th Eur. Conf. Antennas Propag.*, Apr. 2016, pp. 1–5.
[45] T. S. Rappaport *et al.*, "Overview of millimeter wave communications for fifth-generation (5G) wireless networks — with a focus on propagation models," *IEEE Trans. Antennas Propag.*, vol. 65, no. 12, pp. 6213–6230, Dec. 2017.
[46] P. Tang *et al.*, "Millimeter wave channel measurements and modelling in an indoor hotspot scenario at 28 GHz," in *Proc. IEEE 88th Veh. Technol. Conf.*, 2018.
[47] G. R. MacCartney, T. S. Rappaport, S. Sun, and S. Deng, "Indoor office wideband millimeter-wave propagation measurements and channel models at 28 and 73 GHz for ultra-dense 5G wireless networks," *IEEE Access*, vol. 3, pp. 2388–2424, 2015.
[48] C. A. Balanis, *Antenna Theory—Analysis and Design*. Hoboken, NJ, USA: Wiley, 2005.
[49] J. Lota, S. Sun, T. S. Rappaport, and A. Demosthenous, "5G uniform linear arrays with beamforming and spatial multiplexing at 28, 37, 64, and 71 GHz for outdoor urban communication: A two-level approach," *IEEE Trans. Veh. Technol.*, vol. 66, no. 11, pp. 9972–9985, Nov. 2017.
[50] A. Papoulis and S. U. Pillai, *Probability, Random Variables, and Stochastic Processes*. New York, NY, USA: McGraw-Hill, 2002.
[51] O. E. Ayach, S. Rajagopal, S. Abu-Surra, Z. Pi, and R. W. Heath, "Spatially sparse precoding in millimeter wave MIMO systems," *IEEE Trans. Wireless Commun.*, vol. 13, no. 3, pp. 1499–1513, Mar. 2014.
[52] N. Song, H. Sun, and T. Yang, "Coordinated hybrid beamforming for millimeter wave multi-user massive MIMO systems," in *Proc. IEEE Global Commun. Conf.*, Dec. 2016, pp. 1–6.

Shu Sun (S'13) received the B.S. degree in applied physics from Shanghai Jiao Tong University, Shanghai, China, in 2012, and the Ph.D. degree in electrical engineering from New York University Tandon School of Engineering, Brooklyn, NY, USA, in 2018, with a topic on fifth-generation millimeter-wave (mmWave) wireless communications under the supervision of Prof. T. S. Rappaport. She has authored or coauthored more than 40 technical papers in the field of mmWave wireless communications. Her current research interests include mmWave channel models and the analysis of multiple-input multiple-output systems for mmWave channels. She was a recipient of the 2017 Paul Baran Young Scholar Award from the Marconi Society and the 2018 Dante Youla Award for graduate research excellence in Electrical and Computer Engineering in NYU.

Theodore S. Rappaport (S'83–M'84–SM'91–F'98) received the B.S., M.S., and Ph.D. degrees in electrical engineering from Purdue University, West Lafayette, IN, USA, in 1982, 1984, and 1987, respectively. He is the David Lee/Ernst Weber Professor in electrical and computer engineering with the New York University Tandon School of Engineering, New York University (NYU), Brooklyn, NY, USA, and the Founding Director of the NYU WIRELESS Research Center. He founded major wireless research centers with the Virginia Polytechnic Institute and State University (MPRG), The University of Texas at Austin (WNCG), and NYU (NYU WIRELESS), and founded two wireless technology companies that were sold to publicly traded firms. He is a highly sought-after technical consultant having testified before the U.S. Congress and having served ITU. He has advised more than 100 students, has more than 100 patents issued and pending, and has authored or coauthored several books, including the best-seller *Wireless Communications: Principles and Practice-Second Edition* (Prentice Hall, 2002). His latest book *Millimeter Wave Wireless Communications* (Pearson/Prentice-Hall, 2015) is the first comprehensive text on the subject.

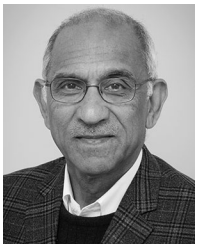

Mansoor Shafi (S'69–M'82–SM'87–F'93–LF'16) received the B.Sc. (Eng.) degree from the University of Engineering and Technology Lahore, Lahore, Pakistan, in 1970, and the Ph.D. degree in electrical engineering from the University of Auckland, Auckland, New Zealand, in 1979. From 1975 to 1979, he was a Junior Lecturer with the University of Auckland, he then joined the New Zealand Post Office, that later evolved to Telecom NZ, and recently to Spark New Zealand. He is currently a Telecom Fellow (Wireless at Spark NZ) and an Adjunct Professor with the School of Engineering, Victoria University. He is a Delegate of NZ to the meetings of ITU-R and APT and has contributed to a large number of wireless communications standards. His research interests include radio propagation, the design and performance analysis for wireless communication systems, especially antenna arrays, MIMO, cognitive radio, and massive MIMO and mmWave systems. He has authored more than 100 papers in these areas. He was a corecipient of two IEEE prize winning papers: the IEEE Communications Society, Best Tutorial Paper Award, 2004 (coshared with D. Gesbert, D.-S. Shiu, A. Naguib, and P. Smith) for the paper "From Theory to Practice: An overview of MIMO Space Time Coded Wireless Systems," IEEE JSAC, April 2003, and the IEEE Donald G Fink Award 2011, (coshared with A. Molisch and L. J. Greenstein), for their paper in IEEE Proceedings April 2009, Propagation Issues for Cognitive Radio. He was also a recipient of the IEEE Communications Society Public Service Award, 1992 for leadership in the development of telecommunications in Pakistan and other developing countries, and was made a member of the New Zealand Order of Merit, Queens Birthday Honors 2013, for services to wireless communications. He has been a Co-Guest Editor for three previous JSAC editions, the IEEE PROCEEDINGS, and the IEEE COMMUNICATIONS MAGAZINE, and a Co-Chair of the ICC 2005 Wireless Communications Symposium, and has held various editorial and TPC roles in the IEEE journals and conferences.

Pan Tang received the B.S. degree in electrical information engineering from the South China University of Technology, Guangzhou, China, in 2013, and the M.S. degree, in 2015, from the Beijing University of Posts and Telecommunications School of Information and Communication Engineering, Beijing, China, where he is currently working toward the Ph.D. degree in information and communication engineering. In 2017, he was a Visiting Scholar with the University of Southern California. His current research interests include mmWave channel modelling, V2V channel modeling, and signal estimation.

Jianhua Zhang received the Ph.D. degree in circuit and system from the Beijing University of Posts and Telecommunications (BUPT), Beijing, China, in 2003. She is currently a Professor with BUPT. She has authored/coauthored more than 100 articles in referred journals and conferences and 40 patents. Her current research interests include 5G, artificial intelligence, data mining, especially in massive MIMO and millimeter wave channel modeling, channel emulator, OTA test, etc. She was a recipient of 2008 Best Paper of Journal of Communication and Network. In 2007 and 2013, she was a recipient of two national novelty awards for her contribution to the research and development of Beyond 3G TDD demo system with 100 Mbps@20 MHz and 1 Gbps@100 MHz, respectively. In 2009, she was a recipient of the "second prize for science novelty" from the Chinese Communication Standards Association for her contributions to ITU-R 4G (ITU-R M.2135) and 3GPP Relay channel model (3GPP 36.814). From 2012 to 2014, she did the three-dimensional channel modeling work and contributed to 3GPP 36.873 and she is also the member of 3GPP "5G channel model for bands up to 100 GHz." She was the Drafting Group Chairwoman of ITU-R IMT-2020 channel model.

Peter J. Smith (M'93–SM'01–F'15) received the B.Sc. degree in mathematics and the Ph.D. degree in statistics from the University of London, London, U.K., in 1983 and 1988, respectively. From 1983 to 1986, he was with the Telecommunications Laboratories, General Electric Company Hirst Research Centre. From 1988 to 2001, he was a Lecturer in statistics with the Victoria University of Wellington, Wellington, New Zealand. During 2001–2015, he was with the Department of Electrical and Computer Engineering, University of Canterbury, Christchurch, New Zealand. In 2015, he joined the Victoria University of Wellington, Wellington, New Zealand, as a Professor in statistics. His research interests include statistical aspects of design, modeling, and analysis for communication systems, cognitive radio, massive MIMO, and millimeter-wave systems.